Study of Dalitz Decays from π^0 in $e^+e^- \to \tau^+\tau^-$ Events Recorded by the Belle II Detector as a Control Sample for Dark Sector Search Validation

by

Dhwani Raju Sutariya
Bachelor of Science (Honours), University of Victoria, 2022

A Thesis Submitted in Partial Fulfillment of the
Requirements for the Degree of

MASTER OF SCIENCE

in the Department of Physics and Astronomy

We acknowledge and respect the Lək̓ʷəŋən (Songhees and Xʷsepsəm/ Esquimalt) Peoples on whose territory the university stands, and the Lək̓ʷəŋən and W̱SÁNEĆ Peoples whose historical relationships with the land continue to this day.

Study of Dalitz Decays from π^0 in $e^+e^- \to \tau^+\tau^-$ Events Recorded by the Belle II Detector as a Control Sample for Dark Sector Search Validation

by

Dhwani Raju Sutariya
Bachelor of Science (Honours), University of Victoria, 2022

Supervisory Committee

Dr. J. Michael Roney, Supervisor
Department of Physics and Astronomy

Dr. Robert Kowalewski, Departmental Member
Department of Physics and Astronomy

Abstract

This thesis presents a validation study of Monte Carlo (MC) simulations in the Belle II experiment by comparing simulated data with real experimental data along with the measurement of the Dalitz decay branching fraction (BF). The analysis focuses on the Dalitz decay of the neutral pion, $\pi^0 \to \gamma e^+ e^-$, which serves as a control sample for searches for dark photons in event $e^+e^- \to \gamma[A' \to e^+e^-]$. The neutral pions are from tau pair events where $\tau^+ \to \bar{\nu}_\tau \pi^+[\pi^0 \to \gamma e^+ e^-]$. By evaluating efficiency and purity, we ensure the robustness of event selection, background suppression, and modeling of key kinematic distributions. After applying selection criteria, the computed MC purity is 99.27% with an efficiency of 0.0122, with the final data sample containing 572 events. The Dalitz decay BF is measured to 0.01076 ± 0.00045(stat.), in agreement with the Particle Data Group (PDG) value of 0.01174 ± 0.00035, with a discrepancy of 1.7σ. This study is limited to evaluation of statistical uncertainties on the BF with a discussion on systematic studies as a follow up. These findings provide essential input for improving data-MC agreement in future dark photon searches and improving measurement of the Dalitz decay BF.

Table of Contents

List of Tables

List of Figures

Acknowledgements

I would like to extend my sincere gratitude to:

Dr. Roney, for your invaluable wisdom, guidance, encouragement and patience.

Dr. Kowalewski, for sharing feedback in weekly meetings and patience during thesis review period.

music, or in the words of ABBA, "Thank You for The Music".

Do or do not, there is no try
Yoda

Dedication

To my family and friends,
thank you for always believing in me.

Chapter 1

Introduction

Ever wondered what makes up the medium you are reading this thesis on? What is the fundamental constituent of matter? How does matter interact with each other? The Standard Model of Particle Physics is the theory in which the answers are found[1]. It describes the ultimate particles that matter is made up of and the interactions between them. But ordinary matter only makes up 5% of all the matter in the universe, the rest is regarded to dark matter (27%) and dark energy (68%).

Dark matter is hypothesised to interact with SM particles through a dark photon, analogous to the electromagnetic photon. A team at Belle II collaboration is searching for a dark photon using the Belle II detector data collected at SuperKEKB collider in Japan. This analysis is a study validating the simulation of the detector with a control sample of the neutral pion Dalitz decay contributing to the effort of the search. The Dalitz decay branching fraction (BF) is also measured from the sample where only the statistical error is evaluated.

The agenda of the thesis is as follows: Chap. 1 introduces fundamental physics concepts and the motivation behind this study. It provides an overview of the Standard Model, its limitations, and the relevance of Dalitz decay and dark photon searches. Chap. 2 provides an overview of the Belle II experiment, detailing the SuperKEKB collider, the Belle II detector subsystems, and their role in particle reconstruction. The theoretical framework behind the decay topology and event selection criteria are detailed in Chap. 3. The data and Monte Carlo (MC) agreement for various kinematic variables are compared in Chap. 4 along with measuring the Dalitz decay BF and purity and efficiency of selection. Chap. 5 outlines a list of studies to be performed to account for the systematic uncertainty in the Dalitz decay BF. Finally, Chap. 6 summarizes the key findings of the study.

1.1 Standard Model

1.1.1 The Fundamental Particles

The twelve fundamental *fermions*, spin $\frac{1}{2}$ particles, are divided equally into two categories: six *leptons* and six *quarks* [2]. The two kinds are differentiated by their distinctive characteristics of charge and interaction behavior, amongst other properties. Some known properties of the different types or "flavours" of leptons and quarks are listed in Table 1.1 and Table 1.2, respectively. As discussed in more detail below, leptons and quarks both interact via the electromagnetic and weak interactions, whereas only quarks interact through the strong interaction.

Leptons carry integer charge while quarks carry fractional charge. There are also neutral leptons called neutrinos, ν. Each charged lepton is paired with a corresponding neutrino. Everyone is familiar with the famous lepton flavour which is the electron, the lightest and stable of all leptons. The muon and tau flavours being heavier cousins of the electron are unstable and decay spontaneously, with mean lifetimes of 2.2×10^{-6} s and 2.9×10^{-13} s, respectively, to kinematically allowed lighter particles. Moreover, each fermion has an antiparticle of the same mass and spin, but opposite charge, and opposite magnetic moment relative to the direction of the spin. For the electron e^-, its antiparticle, the positron, is denoted e^+, and similarly for the muon and tau. The anti-neutrinos are generically denoted $\bar{\nu}$ with corresponding flavour in the subscript.

Interactions between fundamental particles involve certain rules that must be followed for it to be viable. One such law is the *conservation of electric charge* which states that the total charge before the interaction must equal that after the interaction. For example, in the decay of a muon to an electron, $\mu^- \rightarrow e^- + \bar{\nu}_e + \nu_\mu$, the total charge of the system before decay, that of the muon, is -1 which is equal to the total charge of the decay products since the neutrinos have no charge. Each lepton is also assigned a unique *lepton number* (L), 1 for all the particles in Table 1.1 and -1 for its anti-particles and 0 for all other particles. Similarly to the conservation of electric charge, all interactions must preserve the lepton number, this is the law of *conservation of lepton number*.

Protons and neutrons that form the nucleus of an atom were thought to be elementary until they were found to have complex substructure composed of quarks, denoted as "q". As mentioned above, quarks carry fractional charge compared to leptons. But, just like the leptons they are grouped into pairs differing by a unit of charge. Historically, the top t and bottom b quarks were referred to as *truth* and *beauty* while the strange s quark was originally the "sideways" quark [4]. The antiquarks are universally denoted with $\bar{q}$.

Flavour	Symbol	Mass(MeV/c^2)	Electric charge(e)
Electron	e^-	0.5110	-1
Muon	μ^-	105.7	-1
Tau	τ^-	1777	-1
Electron neutrino	ν_e	$< 0.8 \times 10^{-6}$	0
Muon neutrino	ν_μ	< 0.19	0
Tau neutrino	ν_τ	< 18.2	0

Table 1.1: Properties of Leptons. Cosmological arguments state the limit on the total neutrino masses is $0.06 < m_{tot} < 11$ eV while the experimental lower bound is stated above [3].

Flavour	Symbol	Mass (GeV/c^2)	Electric charge (e)
Up	u	$(2.16 \pm 0.07) \times 10^{-3}$	$+\frac{2}{3}$
Down	d	$(4.70 \pm 0.07) \times 10^{-3}$	$-\frac{1}{3}$
Charm	c	1.2730 ± 0.0046	$+\frac{2}{3}$
Strange	s	$(93.5 \pm 0.8) \times 10^{-3}$	$-\frac{1}{3}$
Top	t	172.57 ± 0.29	$+\frac{2}{3}$
Bottom	b	4.183 ± 0.007	$-\frac{1}{3}$

Table 1.2: Properties of Quarks

While leptons can exist singly, by themselves, an isolated quark is not yet observed. They are always confined by the strong interaction in compound systems due to the phenomenon of *quark confinement*. The most elementary quark systems are *baryons*, bound states of three quarks (qqq, $\bar{q}\bar{q}\bar{q}$), and *mesons*, composed of a quark and an antiquark ($q\bar{q}$). Examples of some light mesons and their quark contents are listed in Table 1.3. More rarely, they can also combine into four-quark and five-quark particles, or "tetraquarks" and "pentaquarks" [5]. These quark systems are generically called *hadrons*. Protons (uud) and neutrons (udd) are the lightest baryons but the former is the only stable baryon. The neutron being a little more massive than the proton decays to a proton along with an electron and an anti-electron neutrino, $n \rightarrow p + e^- + \bar{\nu}_e$, and has a mean life of about 15 minutes. All mesons are unstable with the lightest being the pion, π. We discuss the neutral pion in detail in Section 1.3.

Why are only certain combinations of the quarks and antiquarks allowed? What about qq or $q\bar{q}q$? Thanks to *colour*, a further degree of freedom for the quarks. Colour is the strong interaction analog of electric charge. Each flavour of quark comes in three different colours. This has nothing to do with the colours of everyday life and is just based on the analogy that all colours are made from three primary colours. The three colours of the quarks are red R,

Meson	Symbol	Quark Content
Pion (charged)	π^+	$u\bar{d}$
	π^-	$d\bar{u}$
Pion (neutral)	π^0	$\frac{1}{\sqrt{2}}(u\bar{u} - d\bar{d})$
Kaon (charged)	K^+	$u\bar{s}$
	K^-	$s\bar{u}$

Table 1.3: Light mesons and their quark content

blue B and green G and those of the antiquarks are antired $\bar{R}$, antiblue $\bar{B}$ and antigreen $\bar{G}$. We assert that only "colourless" or "white" states of particles are observed and we can resolve this query. Now, only certain combinations of quarks and antiquarks can produce colourless states: $RGB, \bar{R}\bar{G}\bar{B}, R\bar{R}, G\bar{G}, B\bar{B}$.

Similarly to the conservation of lepton number, for interactions involving quarks, the baryon number is conserved. It is defined as B $= \frac{1}{3}(N_q - N_{\bar{q}})$, where N_q is the number of quarks and $N_{\bar{q}}$ is the number of antiquarks. For example, in the neutron beta decay, $n(B = 1) \rightarrow p(B = 1) + e^-(B = 0) + \bar{\nu}_e(B = 0)$ total B before $= 1$ and total B after is $= 1$.

1.1.2 The Interaction Mediators

The SM explains three of the four fundamental forces at work in nature. The elementary fermions interact with each other through fields and the particles associated with these interaction fields are *bosons*, which have integer spin. These mediators or force carriers are listed in Table 1.4. Graviton, the quanta for gravitational force is not yet observed and hence is not included in the SM.

Force	Mediator	Relative Strength	Range
Strong	Gluon (g)	1	$\sim 10^{-15}$ m
Electromagnetic	Photon (γ)	$\sim 10^{-2}$	∞
Weak	$W^{\pm}, Z^0$	$\sim 10^{-6}$	$\sim 10^{-18}$ m

Table 1.4: Mediators of the Fundamental Forces [6].

The *Strong* force is what binds the quarks in protons, neutrons and other hadrons. It also holds the protons and neutrons together inside the nucleus. The particle that mediates this interaction between quarks is the gluon. It has no mass and like the quarks carries a colour charge bringing the total number of gluons to eight. This the strongest of the forces

and operates at the scale of an atomic nuclei.

The *Electromagnetic* force governs the electric and magnetic interactions. This interaction is possible due to the maseless photon. All electrically charged particles, whether quarks, charged leptons, or the $W^{\pm}$, interact through this force. For example, Coulomb scattering between two electrons and absorption of a photon by an electron in an atom. This interaction has infinite range but moderate strength.

The *Weak* interaction is carried by the massive $W^{\pm}$and Z^0 bosons. They have a mass of 80.3692 ± 0.0133 GeV and 91.1880 ± 0.0020 GeV, respectively[1]. This interaction can take place between all quarks and leptons. One key feature is that the W boson can change the flavour of quarks and leptons. This is known as *flavour transition* or *flavour transmutation*. For example, a lepton of one flavour (like an electron) changes into a lepton of a different flavour (like a muon) through the interaction with a W boson. "The Z^0 is (as Saddam would say) the 'mother of all particles', in the sense that it can decay (with a precise calculable probability) into any quark/antiquark or lepton/antilepton pair" [4]. The weak interaction has extremely short range, shorter than the scale of an atomic nuclei and is the weakest force of all due to the massive force carriers.

All this to say that we have an extremely large number of so-called fundamental particles: 12 leptons, 36 quarks, and 12 mediators. But there's just one more, the *Higgs* boson and it plays a very important role of giving mass to all particles [7]. It is named after Peter Higgs, one of the theorists who theorized the existence of the presence of a new field throughout the universe which is associated with the origin of mass. It was discovered in 2012 by the ATLAS and CMS experiments at CERN [8, 9]. In recognition of this groundbreaking discovery, the Nobel Prize in Physics in 2013 was awarded to François Englert and Peter Higgs for their theoretical work on the mechanism that explains how particles acquire mass.

1.1.3 Limitations of The Standard Model

The Standard Model (SM), developed in the 1970's, is an extremely successful scientific theory. It has been successfully tested in thousands of measurements whose fractional precisions reach one part per trillion [10]. However, despite its remarkable success, the SM has several limitations and open questions regarding empirical phenomena that suggests the theory of nature and our understanding of it is incomplete.

- *Gravity* & the *graviton*: The SM does not incorporate gravity, which is described by Einstein's theory of general relativity. Gravity is incredibly weak compared to

[1] c=1 is used going forward for mass and momentum units

the other forces, but it dominates on cosmological scales. The graviton, which is a hypothesized force carrier particle of gravity, has not been observed yet, leaving this force unexplained by the SM.

- *Matter-Antimatter Asymmetry*: If the universe originated from the Big Bang, then matter and antimatter must have been created in equal amounts. But as we know from observations the universe is dominated by matter. There must be some mechanism that kept matter and antimatter from total annihilation, which leads to this realized imbalance. The SM has CPV via CKM matrix, but it is an insufficient amount of CPV to explain this.

- *Dark Matter (DM) & Dark Energy*: The SM is excellent at describing the fundamental particles of nature and their interactions but that's only ordinary matter which accounts for just 5% of the total energy in the Universe. The physics of the remaining 95% is not well conceived. Majority of this inexplicable amount of energy resident in the universe, about 68% is regarded to dark energy, a constant energy density for the vacuum, known for its primary effects of driving the accelerated expansion of the universe. DM will be discussed in more detail in section 1.4. There is ample evidence in astrophysical and cosmological observations for these phenomena but there is no deeper explanation of its nature.

These are just a few mysteries of the nature of the universe that are currently unexplained by the SM. As theoretical research advances and more sophisticated experimental techniques are developed, we should be able to lift the veil of mystery surrounding these phenomena.

1.2 Tau Physics

The heaviest lepton, the τ particle was discovered in 1970 by Perl *et al.* at the Stanford Linear Accelerator Center in California [11]. At 1777 MeV it is $\sim$ 3500 times more massive than the electron. The tau particle can decay to the lighter leptons but due to its heavy mass it is the only lepton that can decay to hadrons as well and will do this $\sim$ 64.79% of the time. These decays happen through the charged weak current, meaning through the exchange of the $W^{\pm}$ mediator [12]. The main hadronic and leptonic decay modes of tau are listed in Table 1.5.

Electron-positron, e^+e^-, colliders have unmatched precedence for producing tau pair events $\tau^-\tau^+$ which makes them perfect for studying tau particles and their decays [13]. Of particular interest is the fourth decay in Table 1.5, $\tau^- \rightarrow \pi^-\pi^0\nu_\tau$ which has the highest

Decay Mode	Branching Fraction (%)
$\tau^- \to e^- \bar{\nu}_e \nu_\tau$	17.82 ± 0.04
$\tau^- \to \mu^- \bar{\nu}_\mu \nu_\tau$	17.39 ± 0.04
$\tau^- \to \pi^- \nu_\tau$	10.82 ± 0.05
$\tau^- \to \pi^- \pi^0 \nu_\tau$	25.49 ± 0.09
$\tau^- \to \pi^- 2\pi^0 \nu_\tau$	9.26 ± 0.10
$\tau^- \to \pi^- 3\pi^0 \nu_\tau$	1.04 ± 0.07
$\tau^- \to \pi^- \pi^+ \pi^- \nu_\tau$	8.99 ± 0.05
$\tau^- \to \pi^- \pi^+ \pi^- \pi^0 \nu_\tau$	2.74 ± 0.07
$\tau^- \to K^- \nu_\tau$	0.696 ± 0.010
$\tau^- \to K^- \pi^0 \nu_\tau$	0.433 ± 0.015

Table 1.5: Branching fractions of common τ decay modes [3]. The horizontal break differentiates leptonic modes from hadronic modes.

branching fraction. Essentially 1/4 of the tau particles decay to a pair of pions and a tau-neutrino. This actually takes place through an intermediate decay of $\tau^- \to \rho^- \nu_\tau$. The *rho meson*, ρ^- is composed of an anti-up and down quark, $\bar{u}d$ just like the charged pions but has a mass of 770 MeV which is 5.7 times the mass of a pion. Therefore, it can be considered to be an excited state of the pion [14]. The pion has zero angular momentum since its quark constituents spins are anti-aligned while the rho meson has its internal quark spins aligned and has angular momentum of one. Under the influence of the strong colour force, the state with spins aligned has a higher energy which shows up as a larger mass energy. This rho meson decays to a pair of pions, $\rho^- \to \pi^- \pi^0$, almost 100% of the time with a lifetime of 0.44×10^{-23} s. Basic properties of the rho meson are listed in Table 1.6.

Quark Content	$\bar{u}d$
Mass	770 MeV/c^2
Decay width	149.1 ± 0.8 MeV

Table 1.6: Basic Properties of the rho ρ^- meson

1.3 Neutral Pion Physics

In 1935, Hideki Yukawa proposed the existence of a new particle, later called the meson, as mediators of the strong nuclear force [15]. Initially, he predicted the mass of this particle to be between 100-200 MeV. Following this in 1938, the possibility of multiple mesons, including

neutral mesons was introduced [16]. Later, a new charged particle with a mass of ~ 140 MeV was observed in an experiment led by Powell *et al.* in 1947 confirming the Yukawa theory. These were the charged pions, $\pi^{\pm}$. It established a new class of particles, the *mesons* [17]. This paper indirectly hinted at the existence of a neutral meson through nuclear interactions. Observances of a neutral particle decaying to gamma rays from cosmic ray showers in 1949 indirectly hinted at the neutral pion, π^0 [18]. Strong evidence of a neutral meson was found in 1950 by Steinberger *et al.* through proton-proton collisions at the Berkeley cyclotron [19]. In the same year Bjorklund *et al.* provided the first direct measurement of π^0 and confirmed that it almost exclusively decays to two photons with an extremely short lifetime [20]. Properties of π^0 and its two main decay modes are provided in Table 1.7 and Table 1.8.

Quark Content	$(u\bar{u} - d\bar{d})/\sqrt{2}$
Mass	(134.9768 ± 0.0005) MeV/c^2
Mean Lifetime	$(8.43 \pm 0.13) \times 10^{-17}$ s

Table 1.7: Basic Properties of the Neutral Pion π^0

Decay channel	Shorthand	Branching Fraction(%)
$\pi^0 \to \gamma\gamma$	$\pi^0_{\gamma\gamma}$	98.823 ± 0.034
$\pi^0 \to e^+e^-\gamma$	π^0_D	1.174 ± 0.035

Table 1.8: Top two decay channels of π^0

As seen in Table 1.8, π^0 decays electromagnetically to two photons at a staggering rate of $\sim 98.8\%$ leaving the second most common decay channel at a rate of $\sim 1\%$. This comparatively rare mode is called the Dalitz decay. Named after Richard Dalitz who, in 1951, predicted that one of the two photons in the dominant decay ($\pi^0_{\gamma\gamma}$) internally converts into an electron-positron pair [21]. Feynman diagrams for the and full event of interest for the analysis is given below.

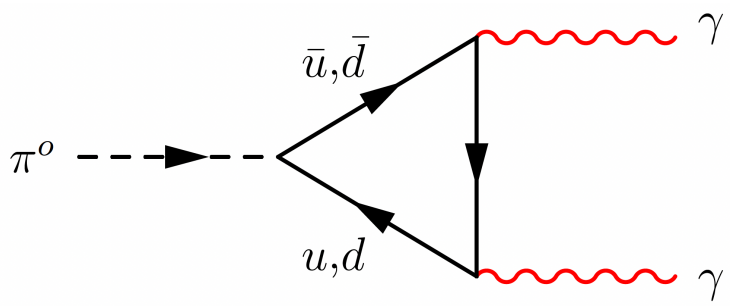

Figure 1.1: Feynamn diagram for the decay $\pi^0 \to \gamma\gamma$

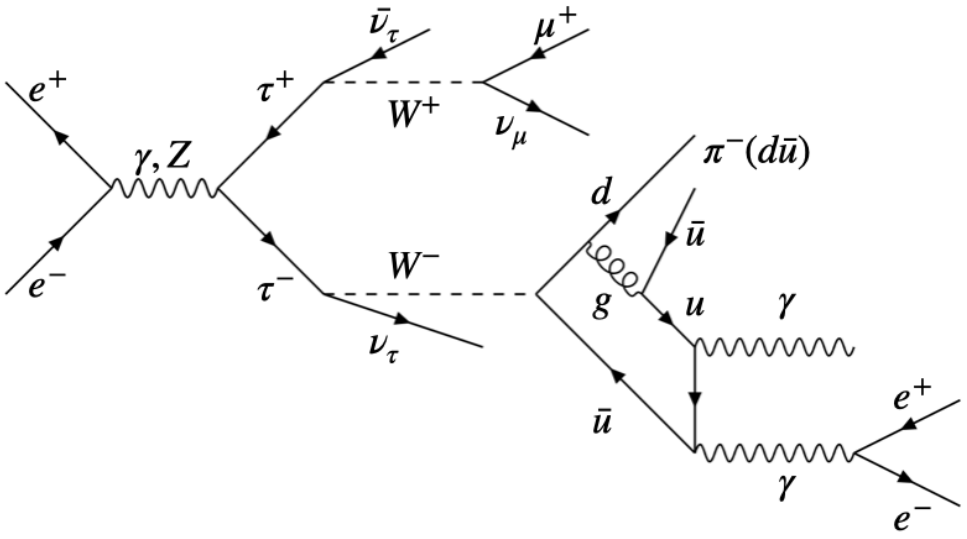

Figure 1.2: Feynamn diagram for the decay of interest

1.4 Dark Matter Mystery

Since time immemorial, philosophers around the world have speculated on the visible as well as invisible forces guiding the dynamics of the universe. Matière obscure, dunkle materie, or DM remains one of the most profound mysteries and elusive subjects in modern particle physics and cosmology. The idea of different forms of matter dates back to ancient natural philosophers like Epicurus (341 BCE -270 BCE) who contemplated that an infinite number of worlds existed, "some like this world, others unlike it" [22, 23]. Furthermore, Galileo's use of the telescope revealed previously invisible celestial objects, such as the moons of Jupiter, reinforcing the idea that the universe contains matter that cannot be seen with the naked eye.

With the introduction of Newton's laws of motion and universal gravitation [24], scientists gained the tools to estimate the mass of astronomical objects based on their dynamics. This led to early predictions of invisible objects, such as John Michell's concept of "dark stars" (now known as black holes). Likewise, DM was also discussed in the form of "dark planets" and "dark clouds".

By the late 19^{th} and early 20^{th} centuries, astronomers like Lord Kelvin and Jacobus Kapteyn began to estimate the amount of DM in the Milky Way using dynamical methods. Lord Kelvin applied the "theory of gases" to the Milky Way arguing that if stars in the Milky Way can be described as a gas of particles, acting under the influence of gravity, then one can establish a relationship between the size of the system and the velocity dispersion of the stars. Following this, in 1906, Henri Poincarè explicitly mentioned DM ("matière obscure" in the original French), and argued that since the velocity dispersion predicted in Kelvin's estimate is of the same order of magnitude as that observed, the amount of DM was likely to be *less* than or similar to that of visible matter [25].

Kapteyn was among the first to offer a quantitative model for the shape and size of the Galaxy, describing it as a flattened distribution of stars, rotating around an axis that points towards the Galactic Pole in doing so he carried out extensive studies of the Milky Way [26]. He found that the apparent movement of stars was not randomly distributed but had two preferential directions: the two star streams. This discovery was later reinterpreted as evidence for galactic rotation. He also suggested that these stellar velocities could be used to find the amount of non-luminous matter in the galaxy. Kapteyn's approach to measuring stellar velocities and density distributions became a foundation for later DM research.

As we have seen, the quantity of DM thought to be present was less than or equal to that of ordinary matter. But we now know that this is not true from the following key

experimental observations leading to strong evidence for the presence of DM.

In 1930's, Fritz Zwicky studied the Coma Cluster of galaxies and applied the virial theorem to estimate its mass [27]. He found that the observed velocities of galaxies within the cluster were much higher than expected based on the visible mass concluding that DM (dunkle materie) must be far more abundant than luminous matter to account for the high velocity dispersion of galaxies in the cluster. This provided evidence for DM at large scales.

In the 1970s, Vera Rubin, along with Kent Ford, studied the rotation curves of spiral galaxies [28]. They measured the velocities of stars and gas at various distances from the galactic center and found that these velocities remained constant (flat) at large radii. From Newtonian law, the rotational velocity of a star should fall when increasing the distance from the Sun. However, the results indicated that the stars farther from the Sun were rotating just as fast as those nearby, showing a flat distribution between the distance and rotational speed. An example of the expected curve (from visible matter) and observed distribution is shown in Fig.1.3. The flat rotation curves indicated that galaxies contain far more mass than could be accounted for by visible stars and gas. This work provided compelling evidence that DM is not just a feature of galaxy clusters but is also present in individual galaxies. These observations were pivotal in convincing the astronomical community of the omnipresence of DM. Her findings, combined with earlier work by Zwicky and others, helped establish DM as a fundamental component of the universe.

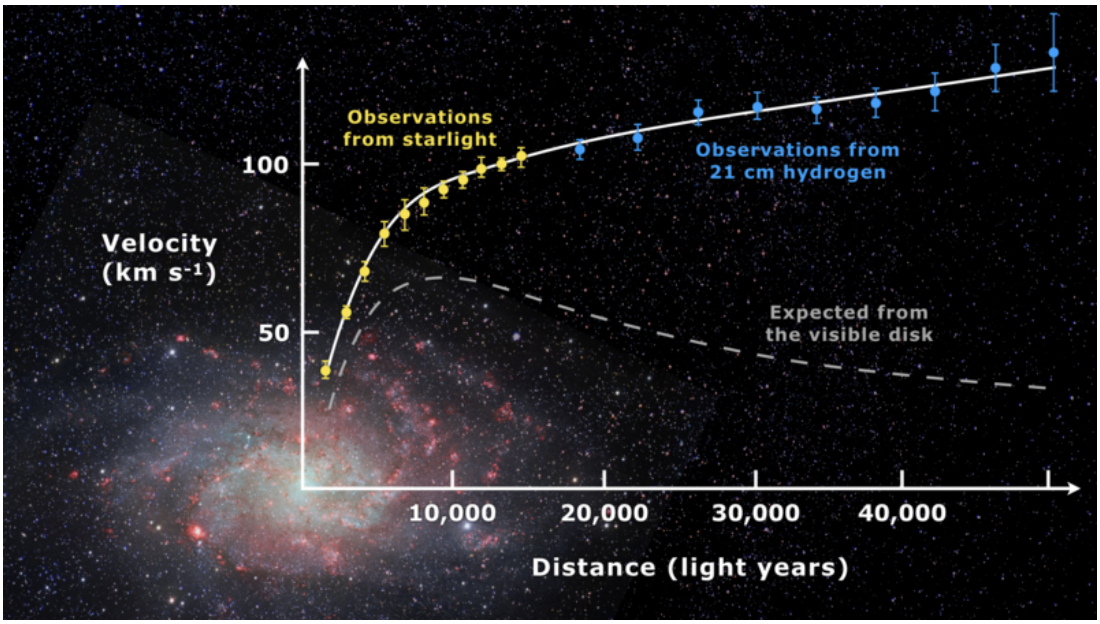

Figure 1.3: Rotation curve of spiral galaxy Messier 33 [29]

Gravitional lensing is a phenomenon predicted by Einstein's theory of General Relativity, where the gravitational field of a massive object (such as a galaxy or galaxy cluster) behaves like a lens and bends the path of light from a more distant object (like a quasar or another galaxy). In effect, leading to magnification, distortion, or multiplication of the images of the background object, providing a powerful tool for studying both the lensing object and the background source.

In 2006, Clowe *et al.* studied the mass distribution of the Bullet cluster, a system of two merging galaxy clusters, through weak gravitational lensing along with X-ray detection and provided additional compelling evidence for the existence of DM [30]. A clear separation was observed between the distribution of baryonic matter (hot gas detected via X-rays using the Chandra X-ray Observatory) and the total mass distribution (inferred from weak gravitational lensing). During the collision, the hot gas, which interacts electromagnetically, was slowed down and concentrated in the center, while the galaxies and the majority of the mass, dominated by DM, passed through relatively unaffected. This separation provided direct empirical proof that DM exists and interacts through gravity, not electromagnetism. Possible explanations with regards to its nature includes hypotheses suggesting that DM interacts through novel, weaker forces beyond the Standard Model.

Cosmic Microwave Background (CMB) is the afterglow of the primordial fireball, the Big Bang. It provides a snapshot of the universe when it was just 380,000 years old. It exhibits small temperature fluctuations (anisotropies) on the order of 1 part in 100,000. These variations in temperature are like ripples on the cosmic pond [31]. By studying these fluctuations we can understand the state of a young universe.

There are three main peaks in the CMB power spectrum. The position of the first peak tells us that the curvature of universe is 0, meaning it is flat and the height tells us about the total matter density. The relative height of the 2nd peak compared to the 1st constrains the baryon density. Initial fluctuations caused matter to gravitationally clump toward regions of higher temperature and density, reinforcing these fluctuations on smaller scales. However, regular matter, which interacts with light, would heat up as it clumped, creating pressure that resisted further collapse. The greater the amount of regular matter, the stronger this pushback effect. As a result, an increased presence of regular matter leads to greater suppression of the second peak in the CMB power spectrum. Therefore, a smaller second peak indicates a higher total matter content in the universe. The properties of the 3rd peak constrain the DM density. DM, like regular matter, gravitationally clumps, but unlike regular matter, it does not interact with light and is unaffected by radiation pressure. While regular matter experiences a pushback due to this pressure, DM clumping remains

unaffected. Consequently, the relative height of peak 3 to peaks 1 and 2 constrains the total DM density [32, 33].

To this effect, the need for DM is clear and the fundamental nature of DM continues to elude us but we know for a fact that it constitutes about 27% of all the matter in the universe and is a form of matter that neither emits, absorbs, nor reflects light, rendering it invisible to electromagnetic observations. Moreover, DM is known to interact only through gravity, without any interactions via the strong or electroweak forces. Despite extensive efforts, we still do not know what DM truly is. Instead, numerous experiments have placed constraints on what DM is not, narrowing down possible candidates but leaving its true identity an open question in cosmology and particle physics.

1.5 Dark Photon

Even though DM doesn't interact with ordinary matter leaving us with no insight about it's nature a fascinating possibility suggests that DM particles could interact with other DM particles via a new *dark force*, much like how ordinary matter experiences the electromagnetic force [34]. If such a force exists, it would be mediated by a hypothetical dark photon, A', which would serve a role similar to that of the ordinary photon in electromagnetism. This exciting prospect has sparked a worldwide race in the search for dark photons.

The minimal DM model relies on a new broken gauge group U(1)' [35]. In this case, the gauge boson, A, couples to the SM hypercharge via kinetic mixing, meaning that the interaction between the dark and SM photon could provide a "portal" through which this hidden sector could be accessed. There are three free parameters in this model, the dark photon mass, the kinetic coupling and the decay branching fraction of the dark photon decaying predominantly into invisible dark-sector final states $A' \to \chi\bar{\chi}$. If such decays are kinematically not allowed then the dark photon will decay into visible SM final states thanks to its suppressed coupling to the electromagnetic current. To measure these properties of the dark photon we need to be able to produce/detect this dark photon at particle physics experiments.

In 2015, researchers at the Institute for Nuclear Research (ATOMKI) in Hungary observed an unexpected excess of events during the decay of an excited state of beryllium-8 (^8Be) [36]. Specifically, they detected more electron-positron pairs than anticipated at a combined energy of approximately 17 MeV. This anomaly led them to propose the existence of a new, light neutral boson, often referred to as the "X17 particle", with a mass around 17 MeV. Experiments at CERN, such as the NA64 and NA62 collaborations, have conducted

searches for the X17 particle but have not observed evidence supporting its existence, placing stringent limits on its possible properties [37, 38]. Moreover, the MEG II collaboration also conducted a search for the hypothetical X17 particle. The analysis revealed no significant signal indicative of the X17 particle. Consequently, the collaboration established upper limits on the branching ratios (relative to gamma emission) for the production of the X17 particle: $R_{17.6} < 1.8 \times 10^{-6}$ and $R_{18.1} < 1.2 \times 10^{-5}$ at a 90% confidence level. These findings do not support the existence of the X17 particle within the sensitivity of the MEG II detector [39].

A search for the dark photons in neutral pion decays was also conducted [40]. The dark photons can be produced at an electron-positron collider like SuperKEKB. The team at Belle II is searching for visible decays of a low-mass dark photon of the type $e^+e^- \to A'\gamma; A' \to e^+e^-$ in a mass range from 10 MeV up to 200 MeV. The focus is on prompt dark photon decay, i.e. probing a kinetic mixing in the $10^4 - 10^3$ range, decay immediately at the production point of the dark photon compared to a displaced decay point.

This analysis is a study contributing to this effort by validating the simulation of the detector with a control sample, $\tau^+ \to \bar{\nu}_\tau \pi^+ [\pi^0 \to \gamma [A' \to e^+e^-]]$, mimicking event characteristics of the signal, i.e e^+e^- from interaction point.

Chapter 2

SuperKEKB & The Belle II Detector

SuperKEKB and Belle II are major upgrades from the Belle/KEKB experiment, located at the High Energy Accelerator Research Organization ((Kō Enerugī Kasokuki Kenkyū Kik)(KEK)) in Tsukuba, Japan. It is aiming for a peak luminosity of 6×10^{35} $\mathrm{cm}^{-2}\mathrm{s}^{-1}$, the highest luminosity ever achieved by a collider, and an integrated luminosity of 50 ab^{-1}.

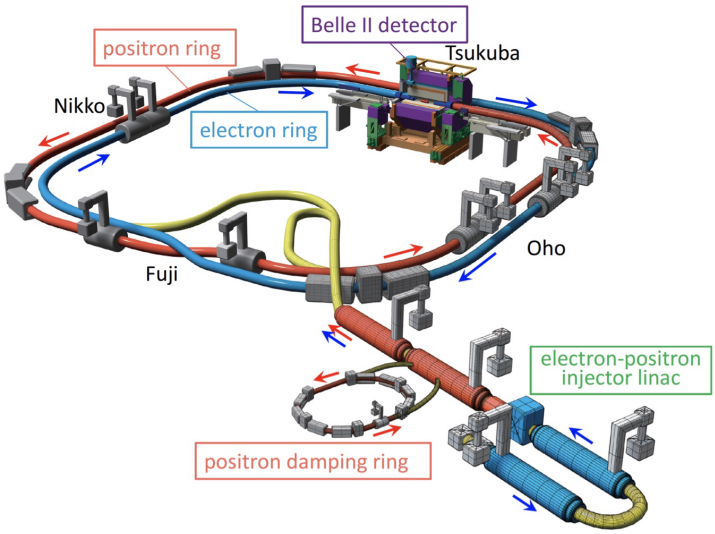

Figure 2.1: Schematic view of SuperKEKB Main Ring [41]

SuperKEKB, shown in Fig. 2.1, is an energy asymmetric collider consisting of a 7 GeV electron ring (the high-energy ring, HER), and a 4 GeV positron ring (the low-energy ring, LER). Its circumference is $\approx$ 3 km [42]. The asymmetric beam energies provide a large enough boost to the centre-of-mass system so that B or D mesons travel an appreciable distance before decaying and thereby allow for precision measurements of lifetimes, mixing parameters, and CP violation [43]. The accelerator is designed to collide electrons and

positrons at centre-of-mass energies in the regions of the Υ resonances (near 10 GeV) [43]. Most of the data will be collected at the $\Upsilon(4S)$ resonance, which is just above threshold for B-meson pair production where no fragmentation particles are produced.

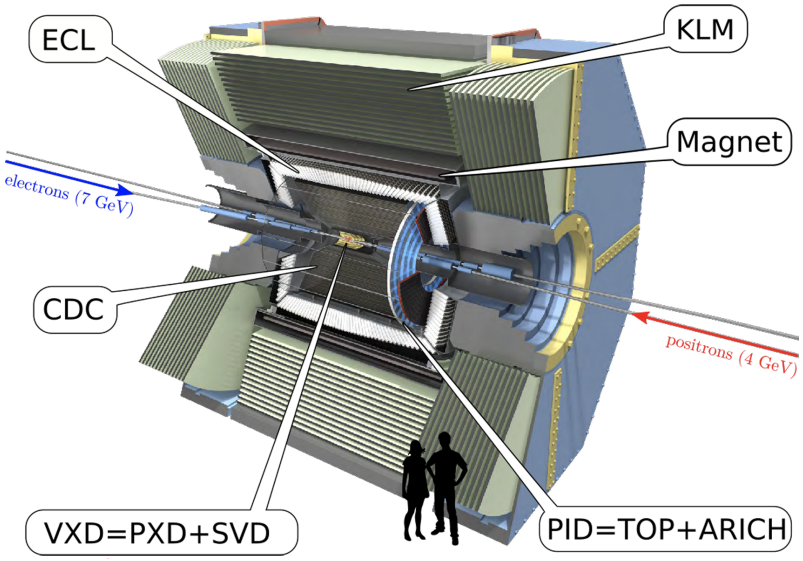

Figure 2.2: The Belle II detector [44]

The Belle II detector, depicted in Figure 2.2, is a multi-layered detector system, much like an onion, consisting of several subdetectors, namely : Pixel Detector (PXD), Silicon Vertex Detector (SVD), forming together the VerteX Detector (VXD), Central Drift Chamber (CDC), Time of Propagation Counter (TOP), Aerogel Ring Imaging Cherenkov Counter (ARICH), Electromagnetic Calorimeter (ECL) and the K-Long Muon System (KLM). PXD, SVD, CDC are inside a soleniodal field of 1.5T. This detector is placed around the electron-positron collision point to collect data produced from the collisions. The various subdetectors are described in following subsections.

2.1 Vertex Detector

The purpose of this sub detector is to collect data conveying precise measurement of decay vertex of B-meson decays, with lifetimes of the order of the picosecond (one trillionth of a second), and of other short-lived particle decays, including charm mesons and tau leptons [45]. The VXD also provides hits on tracks, along with the CDC, which contribute to track reconstruction and therefore to the momentum measurement. Additionally, it offers some dE/dx information.

It is composed of two devices, two inner layers of the silicon Pixel Detector (PXD) followed by four layers of Silicon Vertex Detector (SVD), altogether six layers around a 10 mm radius Beryllium beam pipe. The two layers of the PXD, as seen in Fig. 2.3, at r = 14 mm and r = 22 mm use pixelated sensors. For the data used in this thesis, layer 2 was incomplete with only 2 out of 12 sensors installed. The remaining four layers at radii of 38 mm, 80 mm, 115 mm, and 140 mm are equipped with double-sided silicon strip sensors. Compared to the Belle vertex detector, the beam pipe and the first two detector layers are closer to the interaction point, and the outermost layer is at a considerably larger radius. This results in significant improvement with respect to Belle in the vertex resolution.

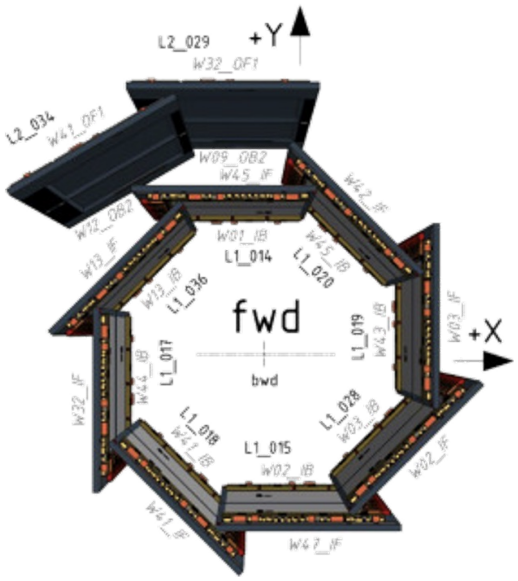

Figure 2.3: The two layers of the PXD [46]

2.2 Central Drift Chamber

The CDC is the central tracking device with the task to reconstruct tracks of charged particles and their momentum, also assist in particle identification by measuring the energy loss.

It is a hollow cylindrical large volume drift chamber with small drift cells and extends out to 1130 mm. The chamber gas is a 50/50 mixture of Helium and Ethane. It contains 14,336 sense wires arranged in 56 layers, either in “axial” (aligned with the solenoid magnetic field) or “stereo” orientation (skewed with respect to the axial wires). This setup allows for reconstruction of a full 3d helix track by combining information from axial and stereo layers. As charged particles move through the CDC they ionize the gas in the chamber. The resulting ionized electrons drift towards the sensing wires due to the drift field and ionize additional

gas atoms. This creates an electron avalanche and a large electronic pulse is registered. Based on the trajectory in the magnetic field, the particle's charge and momentum can be determined and the ionization per unit length (dE/dx) is used for particle identification [47].

2.3 Particle Identification- TOP & ARICH

Charged particle identification is further accomplished by Time-Of-Propagation (TOP) counter in the barrel region and Aerogel Ring-Imaging Cherenkov detector (ARICH) in the forward endcap region of the Belle II detector [48]. This allows for better kaon and pion seperation. Additionally, ARICH provides discrimination between pions, muons and electrons below 1 GeV/c. The operational principle of TOP and ARICH is that of Cherenkov radiation, wherein a charged particle traversing through a medium with a velocity greater than the speed of light in that medium radiates photons.

Each TOP module is a 2.6 m long, 45 cm wide and 2 cm thick quartz bar. An array of 16 such modules surrounds the outer wall of the CDC. As a charged particle passes through the bar, it emits Cherenkov photons which are internally reflected until they reach the end of the bar where Micro-Channel Plates Photo Multiplier Tubes (MCP-PMT) measure the precise x, y position and time of propagation of the photons. As seen in Fig. 2.4, there is a difference in the Cherenkov emission angle for particles with the same momentum but different masses, and consequently different speeds, which results in a different time of arrival of the Cherenkov photons, this is used to separate hadrons [49].

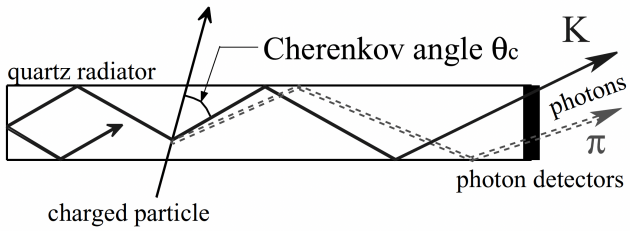

Figure 2.4: An illustrative side-view of emitted Cherenkov photons as charged particles pass through the TOP counter [48]

The proximity focusing ARICH consists of two-layer silica aerogel radiator tiles, each with a thickness of 2 cm and slightly different refractive indices, as seen in Fig. 2.5. As the charged particle passes through the radiator, Cherenkov radiation is emitted. The refractive indices are appropriately chosen so that the two resulting Cherenkov rings can focus and overlap at the photon detector placed 20 cm away from the radiator.

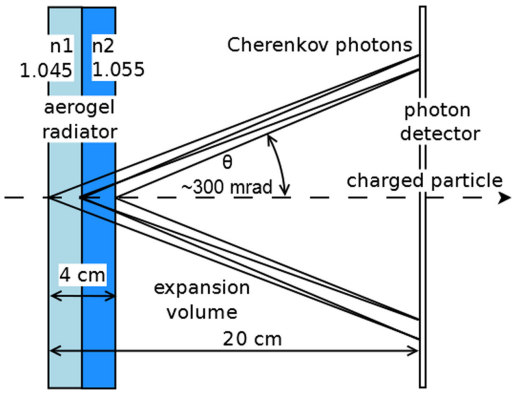

Figure 2.5: Schematic view of the ARICH detector working principle [49]

2.4 Electromagnetic Calorimeter

One third of the B meson decay products are π^0 or other neutral particles that yield photons in a wide energy range from 20 MeV to 4GeV, therefore a high resolution measurement of electromagnetic energy is a very important task of the Belle II detector.

The Electromagnetic Calorimeter (ECL), placed outside the TOP and ARICH counters, detects and determines the energy and angular coordinates of photons as well as helps with the identification and separation of electrons from hadrons. It is composed of a total of 8736 thallium-doped caesium iodide (CsI(Tl)) crystals, of which 6624 are in the barrel (cylindrical part of the detector) and 2112 are in the endcaps (regions at both ends of the barrel, extending coverage to particles emitted at angles along the beam axis), weighing in at a staggering 43 tons. We can see the arrangement of these crystals in Fig.2.6. Each crystal is a truncated pyramid with an average size approximately 6×6 cm^2 in cross section and 30 cm ($16.1X_0$) in length. It covers the polar angle region of $12.4° < \theta < 155.1°$, except for two gaps $\sim 1°$ wide between the barrel and endcaps.

The operational basis of ECL is scintillation. As a particle passes through the crystal, it interacts with the crystal's atomic structure exciting the electrons from the ground state. To return to ground state these electrons emit the excess energy in the form of photons within the visible light spectrum. Two photo-diodes glued to the rear surface of the crystal readout the scintillation light. They are upgraded to include wave-form-sampling as compared to their use in Belle due to the presence of elevated background levels in Belle II introduced with the high luminosity which along with the long decay of the scintillation in the crystals increase the overlapping of pulses from neighbouring (background) events. The photo-diodes were equipped with wave-form-sampling readout electronics to mitigate the resulting large pile-up noise. Futhermore, in the forward region of the detector, close to the beam pipe,

the background rates are expected to be even higher which will only further degrade the performance. To address this challenge in this detector region, the feasibility of replacing CsI(Tl) with pure CsI, which exhibits significantly enhanced response time and radiation tolerance, was investigated and found not to have an impact on the current running of the experiment.

2.5 K-Long & Muon Detector

Located outside the ECL and superconducting solenoid is the K_L^0 and μ (KLM) detector. It's function is to primarily detect and identify long lived neutral kaons and muons.

The structure consists of a layered configuration employing 4.7 cm thick iron plates interspaced with active detector material that surround the barrel and the endcap, as seen in Fig. 2.6. The iron plates serve as the magnetic flux return for the solenoid while providing 3.9 interaction lengths or more of material in which K_L^0 mesons can shower hadronically. The octagonal barrel provides coverage in the polar angle range from 45° to 125°, while the endcaps extend this coverage from 20° to 155°. There are 15 detector layers and 14 iron plates in the barrel and 14 detector layers and 14 iron plates in each endcap. The active detector material is either glass-electrode Resistive Plate Chambers (RPC) or scintillator strips [50]. RPCs are a type of proportional counter based on the principle of ionisation chamber and were used in Belle. They have a long dead time which reduces their detection efficiency significantly under high background fluxes. Therefore, in Belle II RPCs are restricted to the outer layers of the barrel while scintillator strips equipped with silicon photomultipliers were mounted in the two innermost layers of the barrel and in the endcaps, where these backgrounds are expected to be the largest.

Muons with momentum above $\sim$ 0.6 GeV/c traverse the KLM until they range out due to electromagnetic energy deposition or if their momentum is greater than $\sim$ 1.5 GeV/c they pass through all the layers of the KLM and escape the detector. K_L^0 typically undergo hadronic showers in the ECL or the iron plates that can be detected in either the ECL alone, the KLM alone, or both.

2.6 Trigger System

Tasked with the challenging role of discerning between events of interest and background during data taking is the Belle II trigger system. Moreover, a well-conceived trigger system helps access a broad variety of topics not probed in the previous generation B-factories. The requirements of the Belle II trigger system are:

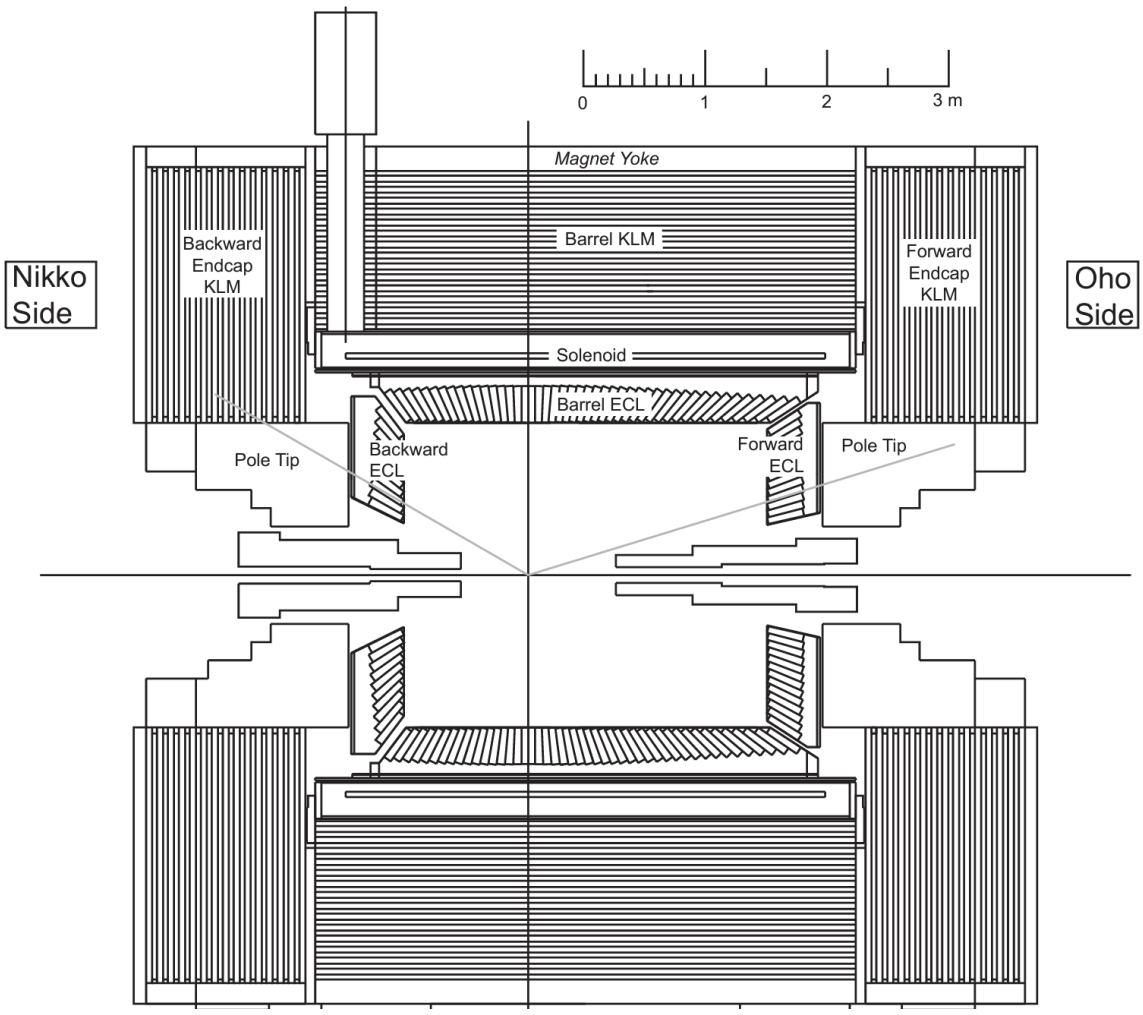

Figure 2.6: Side-view of the Belle II detector showing the arrangement of layers of the KLM in the barrel and endcap [48]

1. High efficiency of hadronic events from $\Upsilon(4S) \rightarrow B\bar{B}$ and from continuum including $c\bar{c}$ events;
    - a low multiplicity trigger for taus, muons and initial state radiation events with small number of tracks;
    - a Bhabha veto is applied but a small sample is retained for calibration purposes;
    - a single photon trigger;
2. a maximum average trigger rate of 30 KHz;
3. a fixed latency of about 5 μs;

4. a timing precision of less than 10 ns;

5. a minimum two-event separation of 200 ns; and

6. a flexible and robust trigger configuration.

The Belle triggering scheme, involving sub-trigger systems and one final decision logic, is updated with new technologies to satisfy the above mentioned requirements of the Belle II trigger system like a Field Programmable Gate Array (FPGA) so that the trigger logic is configurable rather than hard-wired. The sub-trigger systems include:

- *CDC sub-trigger*: Provides charged track information like momentum, positon, charge, and so on.
- *ECL sub-trigger*: Gives energy deposit information, energy cluster information, Bhabha identification, and cosmic-ray identification.
- *Barrel PID (BPID) sub-trigger*: gives precise timing and hit topology information.
- *Endcap PID (EPID) sub-trigger*: gives precise timing information.
- *KLM sub-trigger*: gives muon track information.

Each sub-trigger system is responsible for summarizing trigger information from a specific sub-detector, and sending it to the final-decision logic, which then evaluates combinations of the sub-triggers and issues a trigger if the necessary criteria are fulfilled. The scheme of Belle II trigger system is composed of two levels:

L1: hardware based low level trigger designed to rapidly reduce the event rate to 30 kHz with a latency of 5 μs and a minimum separation between two events of 200 ns. Information from the CDC, ECL, BPID and KLM sub-trigger systems is provided to L1 which is combined using an FPGA based Global Reconstruction Logic (GRL) responsible for performing low level particle and event reconstruction such as matching between tracks detected in the CDC and clusters found by the ECL trigger. Finally, the reconstructed information is received by the Global Decision Logic (GRL) which issues a trigger signal when necessary criteria are met.

HLT: software based high level trigger which is an integral part of the data acquisition system (DAQ). It must identify track regions of interest for PXD readout to reduce

data flux and reduce online event rates to 10 kHz for offline storage. This is achieved by initially suppressing event rate to 15kHz with information from CDC track finding and ECL reconstruction. This typically rejects residual beam background unidentified by the L1. Ultimately, the events passing this step undergo full event reconstruction, with offline reconstruction algorithms using all detectors except for the PXD, further suppressing the rate to 10 kHz.

2.7 Belle II Analysis Software Framework

Given the sheer quantity of data generation at Belle II , a reliable and streamlined framework for data analysis, the Belle II Analysis Software Framework, or basf2, has been developed. It performs both online and offline data handling. The data recorded or simulation produced is organized into sets of runs of variable duration [51]. Each run contains a sequence of independent events. An event stores measurements of the decay products of the collision or a cosmic ray event. A collection of runs with similar hardware state and operational characteristics is defined as an experiment.

Events are analysed by loading independent processing blocks called modules that perform relatively small tasks. Modules are written in C++ or Python and exchange data by passing information to and from a common object store. The configuration of modules for a specific purpose and their order of execution are defined via a Python interface in what is called the steering script. The modules are executed sequentially within a defined path.

Raw data from detector information is reconstructed to provide physical quantities like track hits and calorimeter clusters. This information can then be used to construct high-level objects such as charged tracks. The low level hit and cell information is then discarded (stored elsewhere) reducing the event size by a factor of approximately 40. The reduced information, including the high-level objects, is then used to determine particle level information such as four-momentum and event shape variables. Ultimately, a set of variables for each physics event is stored to mini Data Summary Tables (mDST) files [50]. These variables are mainly associated with the reconstructed energy and momentum of the particle but, exact variables to be computed and stored are specified by the analyst as required by their physics analysis.

Chapter 3

Analysis

The key objective of this study is to validate the MC simulations by comparing them with real data for the search for a dark photon A' in the decay $e^+e^- \to \gamma[A' \to e^+e^-]$ by analysing decays similar to that of A', the neutral pion Dalitz decay, $\pi^0 \to \gamma[A' \to e^+e^-]$. In my notation, A' is primarily used for labeling purposes to denote the virtual photon that then converts internally into the e^+e^- pair. More commonly, one would use γ^* to denote a virtual photon. This is discussed more in Section 3.2. We can do this because the Dalitz decay is similar to the prompt decay of the dark photon. Both of the decays have the same final-state products, $e^+e^-\gamma$, and are mediated by a virtual photon that converts to e^+e^- at the π^0 decay point. This will be done by ensuring that the event characteristics, including vertex distributions, momentum spectra, and background suppression, are well modeled. This analysis will also provide a groundwork for a future search for dark photons and precise measurement of the branching fraction for the Dalitz decay through the π^0.

3.1 Dataset

A table summarising the Belle II dataset used in this analysis is provided below:

	Data	MC
Integrated Luminosity	52.1 fb^{-1}	216.2 fb^{-1}
Experiment	26	26
Sample	bucket 35,36 (excluding some runs)	taupair `MC15rd_b`

Table 3.1: Dataset used in this analysis.

This analysis uses only 52.1 fb^{-1} of the available 424 fb^{-1} Belle II dataset since it is used for validation and estimation of data-MC disagreement and uncertainties. I randomly

selected a small sample of runs from the list of file names from the dataset searcher (excluding 0.7 fb^{-1} of the available bucket 35+36). Data is collected for a given amount of time, typically two weeks (colloquially called a "bucket"), then it is calibrated and processed, and then the process is iterated [52]. Bucket 35 refers to data collected in runs 33-1409 during run period 2022a, where "a" refers to time period Feb-June and bucket 36 is for runs 1410-1968 collected in 2022a.

The MC used is only the taupair sample meaning it contains only events where the initial e^+e^- collision yields $\tau^+\tau^-$, taupair events. These events are generated using the precision Monte Carlo event generator *KK* for two-fermion final states in e^+e^- collisions [53]. The generated events are processed using the standard Belle II detector simulation, which utilizes the `GEANT4` framework to model the passage of particles through matter, including interactions with matter and signal formation [54]. This results in simulated data that matches the format of experimental data.

3.2 Decay Topology

I am interested in studying events in which one of the $\tau^+\tau^-$ decays to $\tau^+ \to \bar{\nu}_\tau \pi^+[\pi^0 \to \gamma e^+ e^-]$ like the signal hemisphere in Figure 3.1 and the tag τ^- undergoes a pure leptonic decay, $\tau^- \to \nu_\tau \bar{\nu_\mu} \mu^-$. Charge conjugates of these decays are implied, meaning that for every decay of a particle, we also assume the equivalent decay of its antiparticle. This follows from the principle that for every fundamental particle, there exists a corresponding antiparticle with the same mass but opposite charge (and other quantum numbers). For example, the antiparticle τ^+ of the tag τ^- undergoing $\tau^+ \to \mu^+ \nu_\mu \bar{\nu}_\tau$ is also considered.

To facilitate the understanding of Figure 3.1 and the following discussion on event selection, let us discuss the concepts of thrust and signal and tag hemispheres.

A pair of τ leptons is produced following a e^+e^- collision via an electromagnetic process mediated by a virtual photon or Z boson. In the center-of-mass frame, these leptons move in opposite directions with equal energy, approximately 5 GeV each, which corresponds to half of the collision energy. The τ leptons are charged particles with a mass of 1.8 GeV/c^2, roughly 3,500 times that of the electron and an average lifetime of approximately 0.3 ps. Therefore, after traveling a few tens of μm, they decay into lighter particles, which are collimated along the τ's original flight direction.

This back-to-back production and the collimated nature of the decays allow for the identification of two distinct spatial regions in the center of mass frame known as hemispheres. A hemisphere is defined as the portion of event space separated by a plane perpendicular

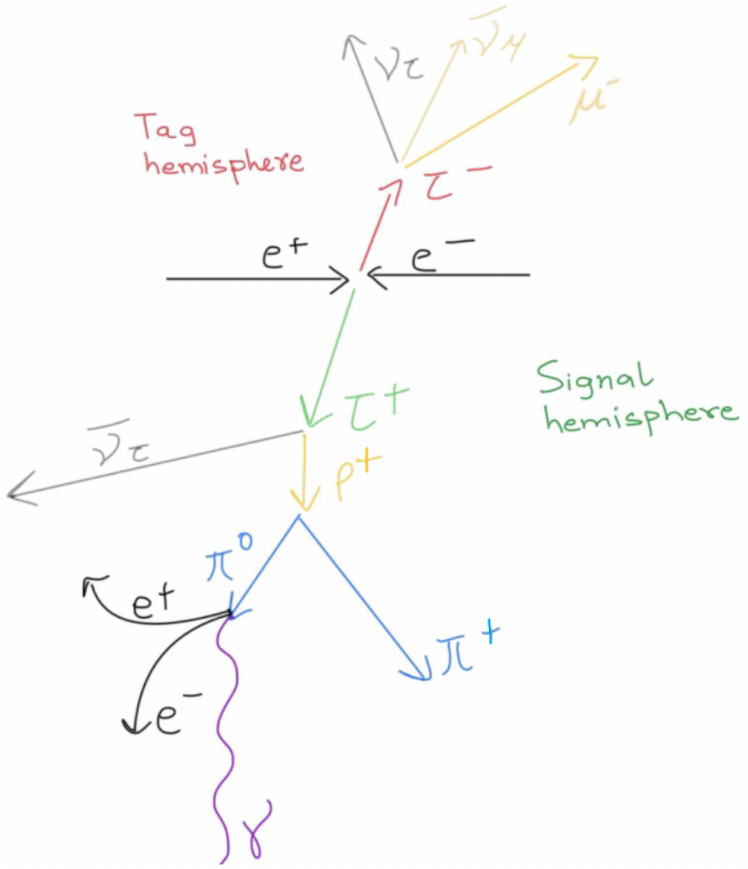

Figure 3.1: Decay Topology

to the τ lepton's motion and passing through the interaction point. These two regions are referred to as the signal hemisphere and the tag hemisphere. The signal hemisphere contains the decay of interest, specifically $\tau^+ \to \bar{\nu}_\tau \pi^+ [\pi^0 \to \gamma [A' \to e^+ e^-]]$, while the tag hemisphere consists of the remainder of the event, including the decay of the other τ lepton.

Although the tag hemisphere does not contain the signal particles, it provides valuable information that helps impose kinematic constraints on the signal and suppress background events. In this analysis, to suppress background processes from the beginning, an exclusive requirement for leptonic decay of the τ tag to μ during reconstruction is employed. While this choice reduces the overall signal sample size, it is expected to significantly enhance background suppression.

The direction of the tau motion can be approximated using the thrust axis. The thrust axis is the unit vector along which the total projection of particles' momenta is maximal [55]. It is the best proxy for the main symmetry axis of the event. The thrust is the normalized sum of projections of all detected particles' momenta onto the thrust axis. It is close to 1 for

a jet-like event, and close to 1/3 for a spherical one. The calculation of the thrust axis allows the event to be divided into two hemispheres. For a set of N particles with momenta p_i the thrust axis $\vec{T}$ is defined as the unit vector along which their total projection is maximal. The thrust scalar is [56]

$$T = \frac{\sum_{i=1}^{N} |\vec{T} \cdot \vec{p}_i|}{\sum_{i=1}^{N} |\vec{p}_i|}$$

3.3 Event Selection

This chapter details the constraints applied on kinematic observables to aid in selection of desired events.

A *steering* script is prepared specifying the decay channels to be reconstructed with constraints on its kinematic quantities along with the observables to be stored using the *basf2* software modules and is run over data and MC samples. In this process, from a huge volume of data stored at the mDST level, variables that are particular to our analysis are selected and stored at the *nTuple* level, reducing file size and making data access efficient. This is the *preselection* sample.

Once information regarding the particles' kinematic properties is available we can streamline the selection further by applying additional selection criteria to improve purity, by removing the background and to bring data & MC distributions into agreement making sure that MC models the experimental data accurately. Details regarding the preselection and additional cuts are discussed in Sec. 3.3.1 and Sec. 3.3.2, respectively.

3.3.1 Preselection

The steering script is attached for reference in Sec. A.1. The following discriminating observables are used to reconstruct events and to identify signal and tag events from background events.

- **Track quality:** $dr \leq 1.0$ cm, $-5.0 \leq dz \leq 5.0$ cm, $nCDCHits > 0$
- **Photon quality:** $E > 0.200$ GeV, $-0.8660 < \cos\theta < 0.9563$
- **Track multiplicity passing quality cuts:** 4 (e^+, e^-, π^+, μ^-)
- **Photon multiplicity passing quality cuts:** 1

- **Event charge neutrality:** Total charge = 0
- **Muon ID threshold using Belle II likelihood method [43]:** > 0.95 (with correction)
- **Track Momenta scale factor**
- π^0 **signal mass:** between 0.08 and 0.20 GeV. See Fig. 3.2a for the distribution.
- τ **signal mass:** < 1.8 GeV
- **Opposite thrust direction** for signal and tag side
- **High-Level Triggers:** L1Trigger = 1, HLT = 1
- **Vertex fitting using vertexTreeFit:** IpConstraint = False

Firstly, a reconstructed particle trajectory must have a transverse impact parameter, dr, of at most 1.0 cm and a longitudinal impact parameter, dz, between -5.0 cm and 5.0 cm. Additionally, it must have at least one hit in the central drift chamber, ensuring that it is well-reconstructed. Exactly 4 charged particle tracks must be present in the event, one for each of e^+, e^-, π^+, μ^-. A standard Belle II correction factor is applied to the measured track momenta for calibration purposes as shown in line 59 of the steering script in the Appendix A.

The photon energy must be greater than 0.200 GeV, and its polar angle θ must be in the fiducial region. There must be exactly 1 reconstructed photon passing those criteria in the event, this is tricky due to beam induced background and cluster split-offs.

The sum of all detected particle charges in the event must be zero, ensuring charge conservation. A particle is identified as a muon if its likelihood of being a muon compared to other particles is greater than 0.95 (after applying a correction). The invariant mass of a neutral pion reconstructed from γ, e^+ and e^- must be within the range 0.08–0.20 GeV to ensure it is correctly identified. The reconstructed invariant mass of the signal-side τ decay must be less than 1.8 GeV. The signal-side and tag-side τ decays must have opposite thrust directions, ensuring a valid event topology. Events must pass specific trigger conditions, the Level-1 Trigger (L1Trigger) and High Level Trigger (HLT). A vertex fitting algorithm treeFit, for e^+, e^- is used, but without applying an interaction point constraint [57].

3.3.2 Additional Selection

Once we have the reconstructed observables in the nTuple we can apply further cuts to optimize our selection of Dalitz decays.

- **A' constraints**
  - Center of mass frame $cos\theta < 0.75$
  - Invariant Mass < 0.3 GeV
- **e^+ and e^- constraints**
  - Both e^+ and e^- track's electron identification threshold is > 0.2
  - At least one of the e^+ and e^- track's electron identification threshold is > 0.9
  - Both e^+ and e^- tracks have atleast 1 PXD hit

The following are *final cuts* applied to increase purity of selected Dalitz sample by suppressing background and to bring data-MC into better agreement.

- Transverse momentum of both e^+ and $e^- > 0.3$ GeV
  - Ensures the e^+ and e^- tracks make it to the ECL so that the ECL is used in PID.
- A' transverse vertex distance assuming it's a converted photon < 0.5 cm. This distance is computed under the assumption that A' has 0 mass. By construction this distance is constrained to be non-negative.
  - Suppresses the conversion in material which is main source of background
- A' transverse vertex distance between $<$ 1cm. By construction this distance is constrained to be non-negative.
  - removes additional background conversion events

The distribution of π^0 mass after each of the three selection stages mentioned above is presented below. The histograms are luminosity normalized.

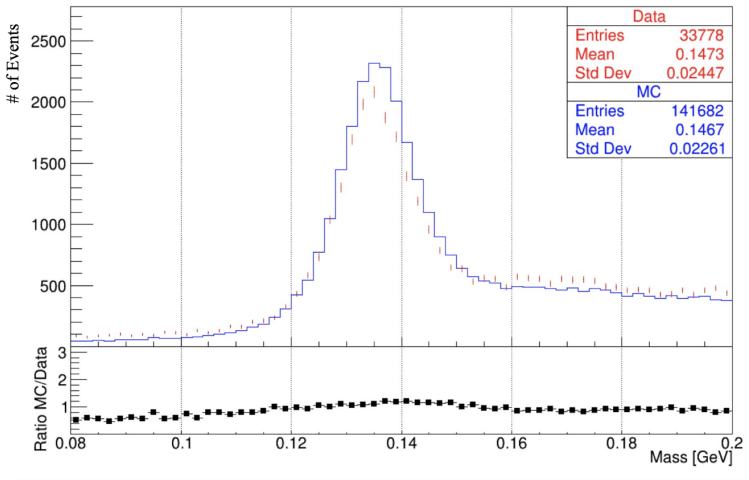

(a) After preselection

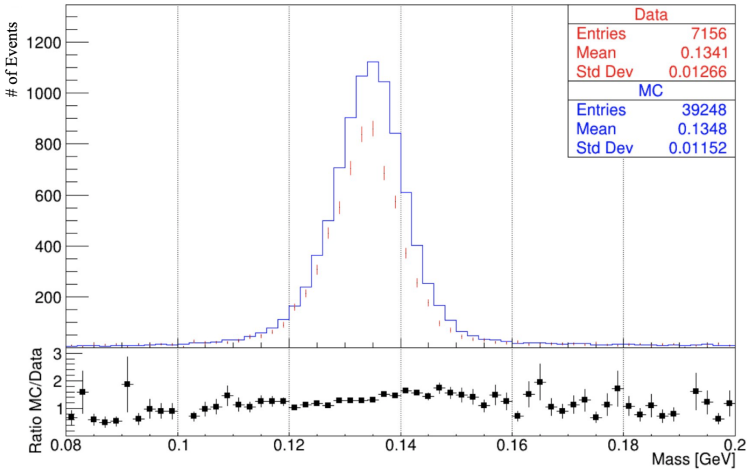

(b) After additional cuts

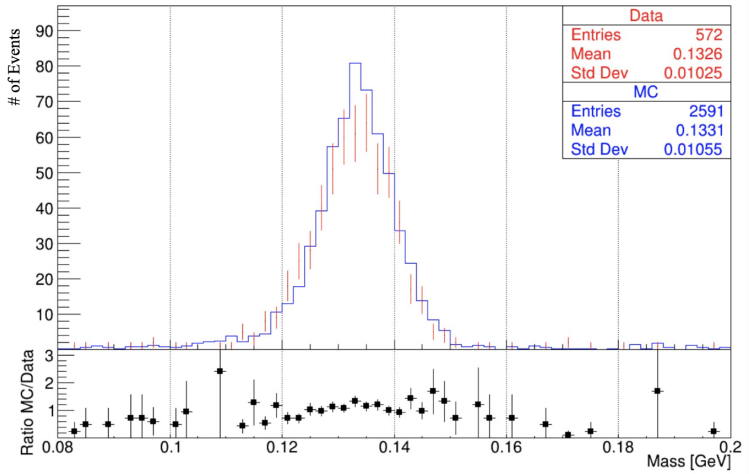

(c) After final cuts

Figure 3.2: Distribution of π^0 mass

Chapter 4

Results

This chapter highlights the essential findings of the analysis. We discuss the data and MC agreement and measure the Dalitz decay ($\pi^0 \to e^+e^-\gamma$ denoted π^0_D) BF along with related statistical uncertainties.

While comparing the data and MC agreement distributions of kinematic observables like the momentum, reconstructed mass of particles, vertex distance from IP among a long list of other variables are generally plotted to check whether the observed distributions match the predicted ones. They are plotted to also gauge aspects of measurements like resolution of energy, distance measurement.

Some very puzzling and important features were discovered in the distribution of observables in the data samples used. Along with good data and MC agreement for Dalitz decay selection with high purity.

Let's start by discussing the puzzling distribution of the A' `transverseVertexDistance`, the distance A' travels in the transverse plane before converting into and e^+e^- pair. In all the following plots the distributions have been luminosity scaled, which means that the number of events in each bin for the MC has been scaled down by a factor 4.15 to match the luminosity of the data. The histogram labelled MC contains the full selection including Dalitz and non Dalitz decays. MC Dalitz is selected by exclusively requiring the mother of the e^+ and e^- to be the pion. This is done by applying the condition `genMotherPDG`=111, the Particle Data Group (PDG) ID for the pion, to both the daughter, e^+ and e^-, candidates. Finally, the data and MC agreement for each distribution is checked by comparing the number of events in each bin between data and MC, this is plotted as the ratio of MC/data in all plots. A ratio of 1 suggests perfect agreement, any deviations from this could suggest background contamination, simulation mis-modeling or statistical fluctuations.

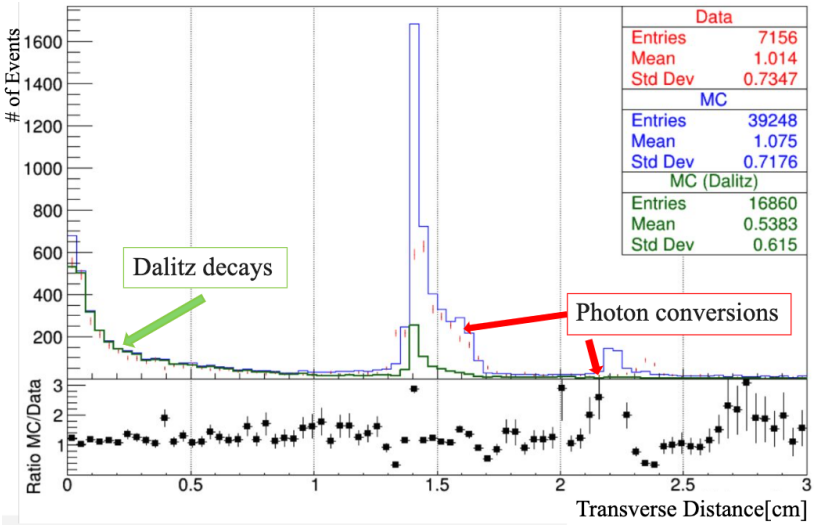

Figure 4.1: Distribution of e^+e^- creation vertex distance in the transverse(x-y) plane

As seen from Fig. 4.1 the location of the Dalitz transition are reconstructed in a manner that is enhanced at two transverse distances in the detector, at 0cm, the interaction point (IP) and at 1.4cm, first layer of the PXD. It is encouraging to see the Dalitz decays at the IP as expected, since they are prompt decays but unexpected is their presence at the PXD layer. Moreover, the data at the second layer of the PXD is peaking at 2.3cm, but the material is at 2.2cm according the design.

By looking at the true MC generator-level distribution of the transverse distance of π^0_D in Fig. 4.2a and $\pi^0_{\gamma\gamma}$($\pi^0 \to \gamma\gamma$) in Fig. 4.2b we can confirm that the π^0_D should all be at the origin.

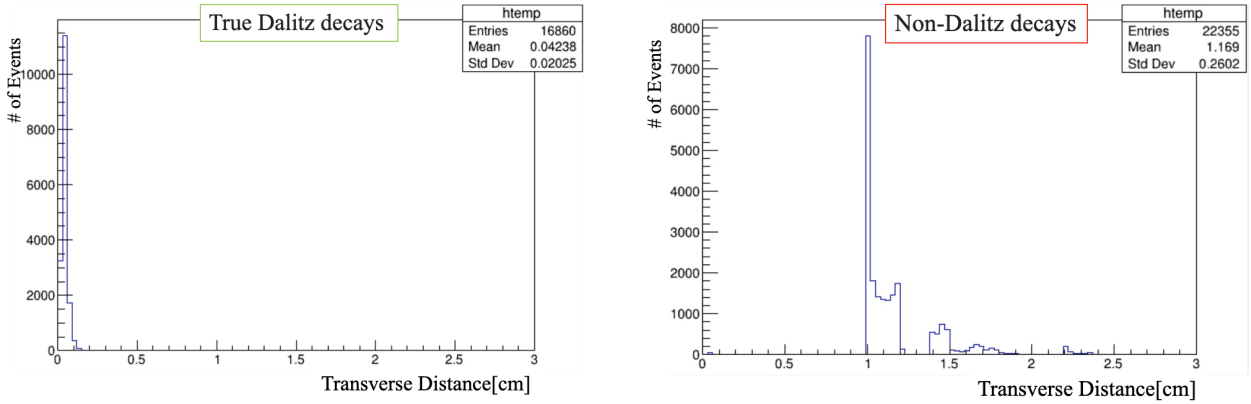

(a) Dalitz decays

(b) Non Dalitz decays

Figure 4.2: Comparison of generator-level transverse vertex distance distributions for Dalitz and Non Dalitz decays.

The $\pi^0_{\gamma\gamma}$, produces conversions of γ to e^+e^- through the interaction in the material of the detector and peak at 1cm while encountering the first material layer of the detector, the beam pipe, but, in Fig. 4.1 peak at the PXD. Clearly, something is not working as it should for our sample of events. There is a bias towards the PXD layer and e^+e^- created at the origin are reconstructed incorrectly near the PXD. There is a disagreement between data and MC background rates from conversions for transverse distances of the vertex >1cm. Consequently, this requires an additional criteria of <1cm to suppress background and reduce disagreement.

To better visualize the transverse vertex distance distribution, the 2-dimension distributions of x vs y distances of the A' vertex is given in Fig.4.3. This maps out the layers of the PXD along with the events at IP. Moreover, we can clearly see the Dalitz decays at the PXD where mostly all the conversions are as seen in Fig 4.3a,4.3c. To avoid visual biases arising from using a higher MC luminosity compared to data, the MC plots have been produced using full MC luminosity along with plots using same luminosity as data.

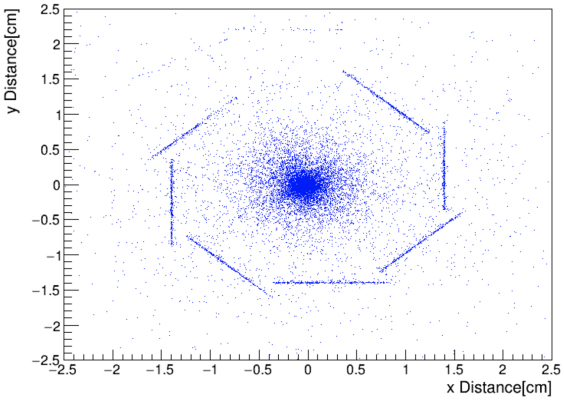

(a) MC Dalitz events only

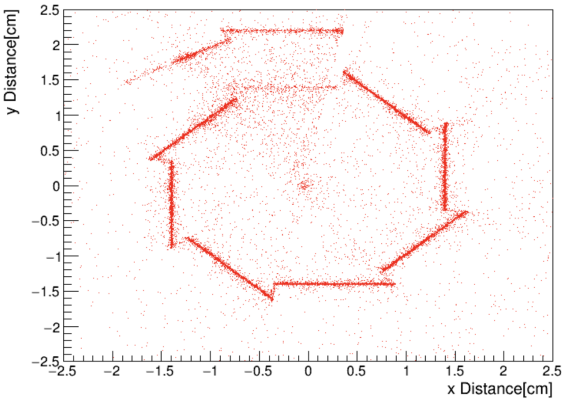

(b) MC non-Dalitz events only

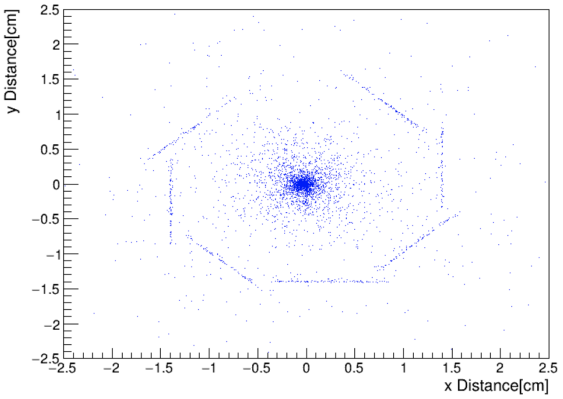

(c) MC Dalitz events only. Note: Effective MC luminosity roughly matches the data luminosity.

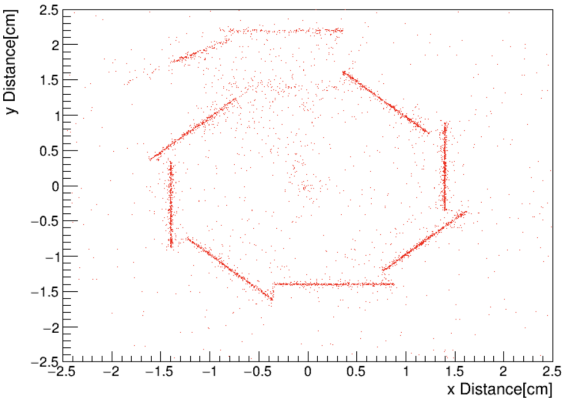

(d) MC non-Dalitz events only. Note: Effective MC luminosity roughly matches the data luminosity.

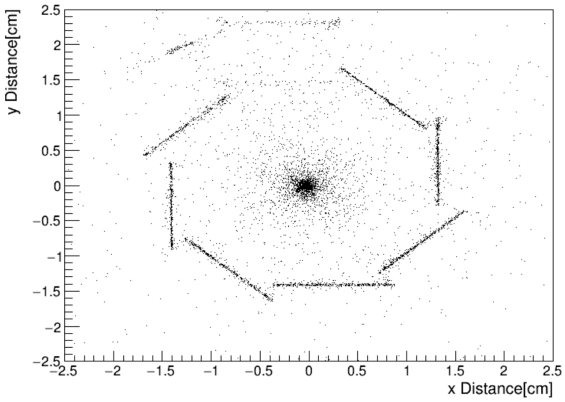

(e) Data

Figure 4.3: Comparison of vertex distributions in the x-y plane for data and MC.

Studies using a `kfit` vertex fitter instead of the `treefit` were also performed to compare the performance on event reconstruction by the two fitting modules. The comparison plot below, Fig. 4.4 shows that `kfit` has even poorer reconstruction resolution than the already

employed `treefit`, this is obvious by the pile up near the origin in the distribution with `kfit`.

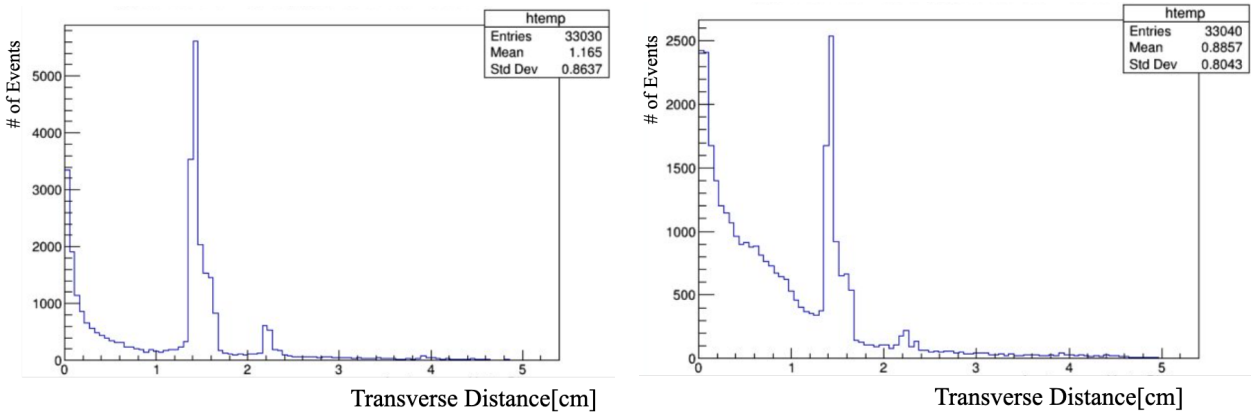

(a) `treefit` (b) `kfit`

Figure 4.4: Comparison of transverse vertex distance distributions using `kfit` and `treefit`.

Let's look at the effect of applying final cuts on event selection to increase purity of the Dalitz selection while supressing background from non Dalitz decays on some distributions. Starting by analysing the distributions before the final cuts are in place.

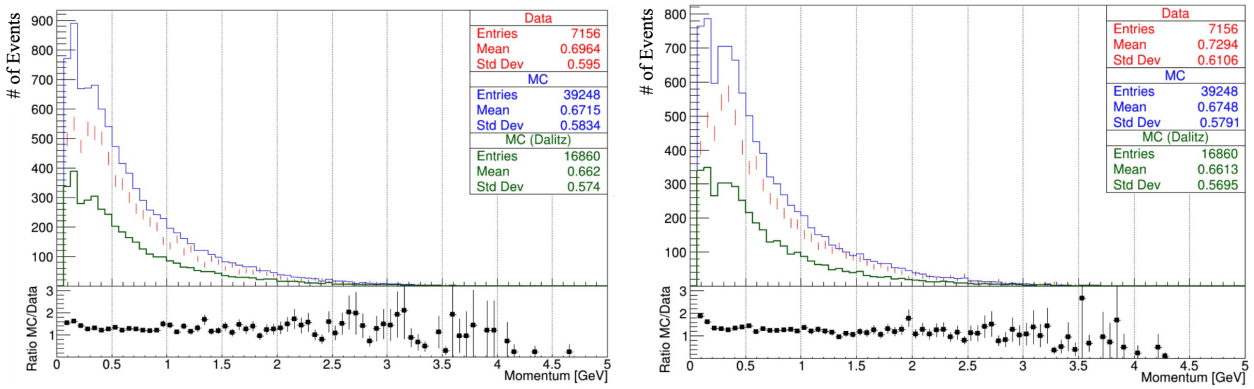

(a) e^+ momentum (b) e^- momentum

Figure 4.5: Distribution of e^+ and e^- momentum before application of final cuts

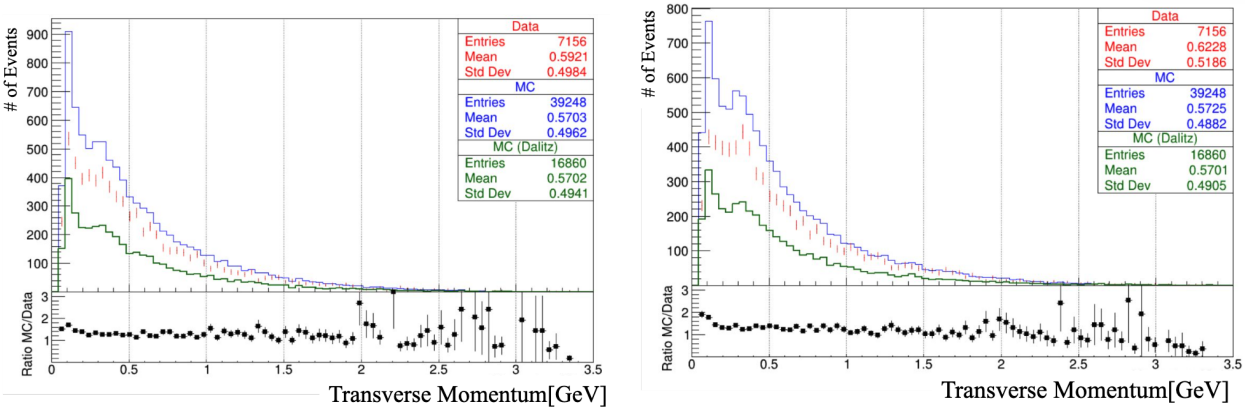

(a) e^+ transverse momentum (b) e^- transverse momentum

Figure 4.6: Distribution of transverse momentum for e^+ and e^- before final cuts.

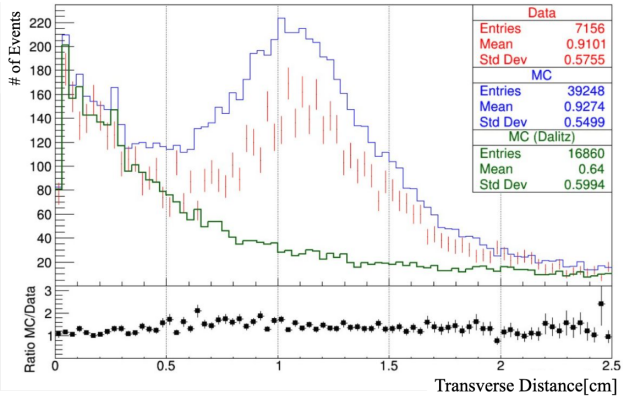

Figure 4.7: Distribution of A' transverse vertex distance assuming its a converted photon before application of final cuts

The transverse momentum distribution for e^+ and e^- in Fig.4.6a and Fig.4.6b show high disagreement between data and MC in the low momentum region, below 0.3 GeV. Analysing Fig. 4.7 showing the distribution of A' transverse vertex distance under the assumption of a converted photon shows high background rate in region $>$ 0.5cm, peaking at 1cm where photon conversion from interaction with material in beam pipe takes place.

Finally, "N-1" plots are generated to validate the final event selection criteria. N-1 plots used to visualize the effect of each selection cut while keeping all other cuts applied. The distribution of the remaining variable is plotted. This is done for each of the 3 final cuts. This helps to check whether the cut on that variable significantly changes the event distribution or introduces biases. Three N-1 plots are presented below. The red line indicates value of the cut.

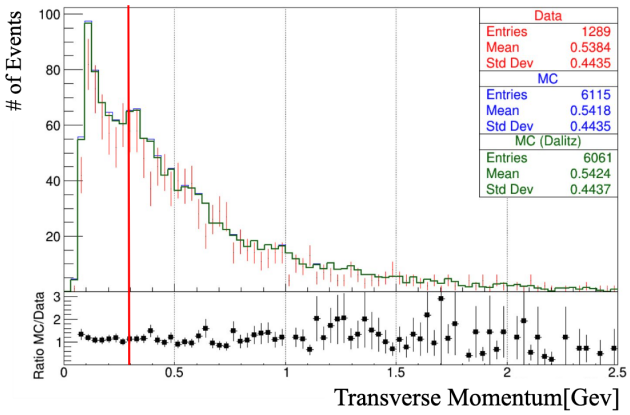

(a) e^+ transverse momentum distribution. Events to the right of the red line are accepted.

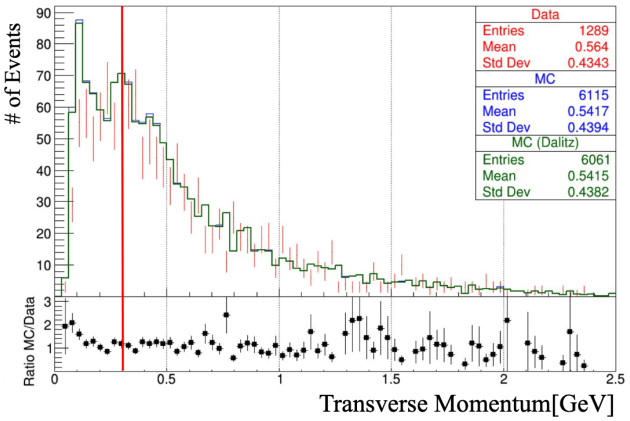

(b) e^- transverse momentum distribution. Events to the right of the red line are accepted.

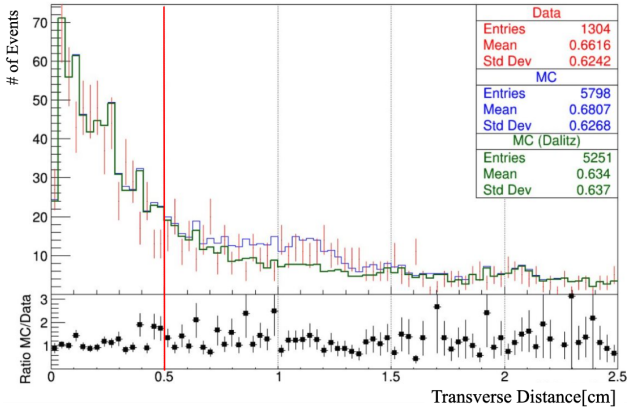

(c) e^+e^- transverse vertex distance assuming its a converted photon. Events to the left of the red line are accepted.

Figure 4.8: N-1 plots

The distributions confirm that the application of the cuts is reasonable as it further suppresses background from $\pi^0_{\gamma\gamma}$ and brings data and MC to good agreement. This calls for revealing the distribution of the observables with final selection criteria applied.

These are presented below.

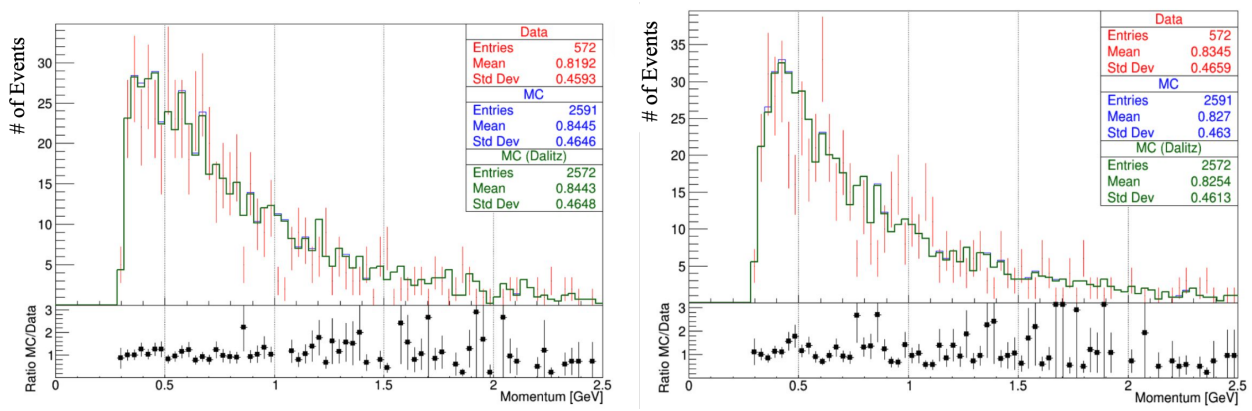

(a) e^+ momentum distribution (b) e^- momentum distribution

Figure 4.9: Comparison of e^+ and e^- momentum distributions after final cuts.

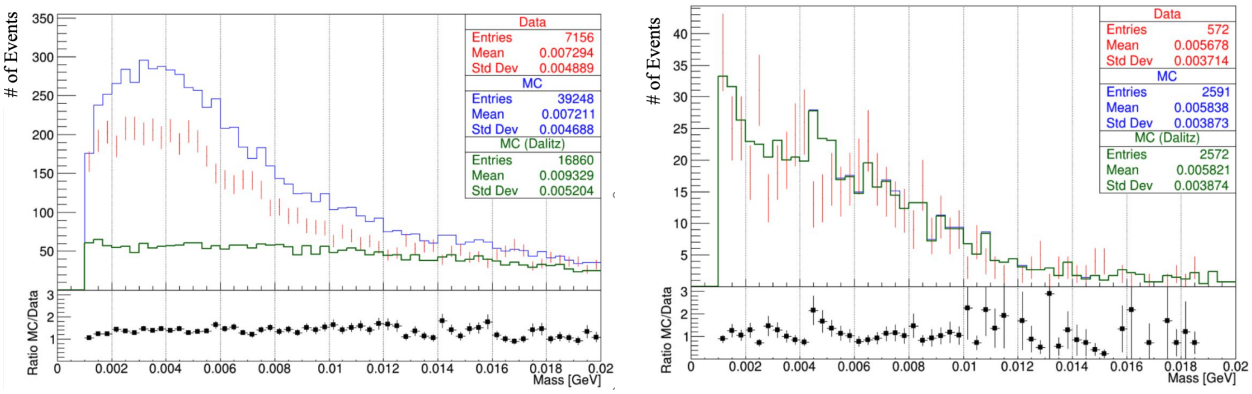

(a) before final cuts (b) after final cuts

Figure 4.10: Comparison of invariant mass distributions of A' before and after final cuts.

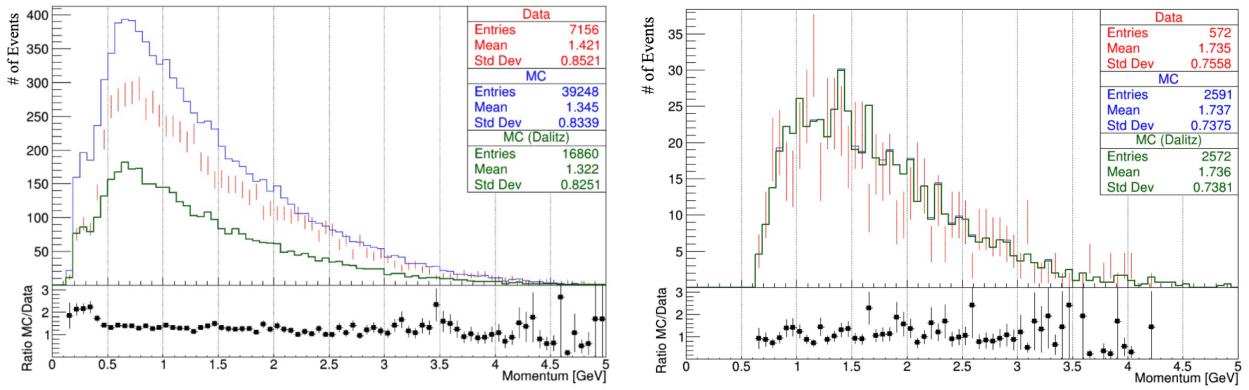

(a) before final cuts

(b) after final cuts

Figure 4.11: Comparison of A' momentum distributions before and after final cuts.

As we can see by comparing the preselection distributions to the final selection that we have achieved a very clean sample of π_D^0 and good agreement between data and MC. We can now quantify the agreement and estimate the π_D^0 BF. A table summarizing the effect of each cut on the number of events in the data and MC samples is provided below.

Cut	**No. of Dalitz Events MC** (normalized to 52.11/fb)	**No. of Non-Dalitz Events MC** (normalized to 52.11/fb)	**No. of Events Data** (in 52.11/fb sample)
No Cuts	50702.62	4318792.52	—
Preselection	6947.68	27198.33	33778
A' constraints	6469.53	24207.70	30326
$e^+$and e^- constraints	4063.34	5395.61	7156
Transverse momentum e^+ and $e^- > 0.3$ GeV	1740.29	2310.99	3362
Converted photon transverse distance <0.5 cm	885.45	84.59	888
A' transverse distance < 1 cm	619.86	4.58	572

Table 4.1: Comparison of number of remaining MC Dalitz events, MC non-Dalitz events, and data events after each cut is applied.

4.1 Dalitz Branching Fraction

Efficiency (ϵ) and purity studies are essential components of validation studies, ensuring the robustness of event selection, background estimation, and MC simulations. By systematically comparing efficiency and purity between MC and experimental data, we can evaluate the effectiveness of event selection while identifying potential discrepancies arising from detector effects, background contamination, or limitations in theoretical modeling. Establishing confidence in these aspects is crucial, as the absence of rigorous validation could introduce biases or systematic errors, ultimately compromising the reliability of any derived scientific conclusions.

Purity (P) quantifies the fraction of correctly identified signal events after selection cuts. It is given by:

$$P = \frac{N_{\text{signal}}}{N_{\text{signal}} + N_{\text{background}}} \tag{4.1}$$

For this analysis, the computed purity in MC is

$$P = (99.27 \pm 0.17)\%$$

Our final sample after applying all selection criteria has a total of 2591 events in MC, out of which 2572 are identified as Dalitz decay events and 19 events are background events, with 572 events in data.

To account for background contributions, the number of background events (N_b) is estimated from MC and scaled to data luminosity. N_b events in MC is 19, and after scaling to the data luminosity, it becomes

$$N_b^{\text{data}} = N_b \times \frac{52.11 \text{ fb}^{-1}}{216.22 \text{ fb}^{-1}} = 4.6 \pm 1.1$$

After subtracting this background from the selected events in data, the number of Dalitz decays is

$$N_{\text{Dalitz}} = N_{\text{selected, Data}} - N_b^{\text{data}} = 572 - 4.58 = 567 \pm 24(\text{data statistics})$$

Now one can measure the Dalitz decay BF from the current sample with this relation:

$$N_{\text{Dalitz}} = \epsilon_{MC} \times N_{\tau^+\tau^-} \times \text{BF}(\tau \to h\pi^0) \times \text{BF}(\tau \to \mu) \times \text{BF}(\pi^0 \to e^+e^-\gamma) \times 2 \tag{4.2}$$

$$\therefore \mathrm{BF}(\pi^0 \to e^+e^-\gamma) = \frac{N_{\mathrm{Dalitz}}}{\epsilon_{MC} \times N_{\tau^+\tau^-} \times \mathrm{BF}(\tau \to h\pi^0) \times \mathrm{BF}(\tau \to \mu) \times 2} \tag{4.3}$$

where,

- ϵ_{MC} is the measured efficiency in MC, it is calculated in following discussion on efficiencies and is found to be 0.0122±0.0002
- $N_{\tau^+\tau^-}$ is the number of tau pair events in 52.11 fb^{-1} of data and is calculated from the $e^+e^- \to \tau^+\tau^-$ cross section which is 0.919nb. Then $N_{\tau^+\tau^-}$ = 47,889,090 events (52.11 fb^{-1} × 0.919nb)
- BF($\tau \to h\pi^0$) is the BF of $\tau \to h\pi^0$ where h is a pion or kaon, it is = 0.2593
- BF($\tau \to \mu$) is the BF of $\tau \to \mu$ and has a value of 0.1739
- the factor of 2 is to account for the fact that we include charge conjugates

Substituting for values, we get the BF as 0.01076 ± 0.00045(stat.) compared to the PDG value of 0.01174 ± 0.00035. The observed difference is 1.7σ taking into account the PDG uncertainty for Dalitz decay BF. Moreover, measuring a BF consistent within statistical errors of the PDG validates the detector MC's description of the data.

Using the MC scaling, the predicted number of Dalitz decays in data is

$$N_{\mathrm{Dalitz,\ predicted}} = 620 \pm 12$$

The observed difference between prediction and data is

$$\Delta N = 620 - 567 = 52,$$

with a data statistical uncertainty of 24 events. This is a relative statistical error on the current amount of dataset is

$$\frac{\sigma_N}{N_{\mathrm{Dalitz}}} = 0.042,$$

while projecting this measurement to using 500 fb^{-1}, it is

$$\frac{0.042}{\sqrt{500/52.11}} = 0.014.$$

The PDG value for the Dalitz decay is 0.01174 ± 0.00035. Therefore, the relative uncertainty is 0.03. With just including statistical uncertainty we project that using 500fb^{-1}

one can achieve half the relative uncertainty of the current world best measurement for the Dalitz decay branching fraction. Including this PDG uncertainty, the discrepancy on predicted Dalitz decay count reduces to 1.6σ, suggesting reasonable agreement between data and MC. This is slightly different from the significance between the PDG and my measurement of Dalitz BF (1.7σ), this is due to accounting of MC stat. error in the former, but not latter.

ϵ quantifies the fraction of true signal events that are successfully selected after applying event selection criteria. It is defined as

$$\epsilon = \frac{N_{\text{selected}}}{N_{\text{total}}} \tag{4.4}$$

where N_{selected} is the number of signal events remaining after all selection cuts, and N_{total} is the total number of signal events in the sample before any selection even before *preselection* is given by:

$$N_{\text{total, MC}} = N_{\tau^+\tau^-} \times \text{BF}(\tau \to h\pi^0) \times \text{BF}(\tau \to \mu) \times \text{BF}(\pi^0 \to e^+e^-\gamma) \times 2 \tag{4.5}$$

where h is a charged pion or kaon, and the factor of 2 is to account for the fact that we include charge conjugates. Substituting the numerical values from the PDG and the $N_{\tau^+\tau^-}$ from the metadata information of the MC using basf2 software:

$$N_{\text{total, MC}} = 198703280 \times 0.2593 \times 0.1739 \times 0.01174 \times 2$$

$$N_{\text{total, MC}} = 210380.3$$

For MC, the efficiency is

$$\epsilon_{\text{MC}} = \frac{2572}{210380.3} = 0.0122 \pm 0.0002(\text{stat.}) \tag{4.6}$$

This is really low, the leading factors that result in a low efficiency are the final cuts. The final cuts not only suppress background but also result in the loss of signal events. The cuts are electron-positron tracks with transverse momentum >0.3GeV, this removes a lot of our signal events. The cut on transverse displacement from conversions < 0.5cm suppresses the conversion in material backgrounds while the transverse displacement cut <1cm removes mis-reconstructed Dalitz at the PXD and the non Dalitz decays.

Since the total number of Dalitz decays in data ($N_{\text{total, Data}}$) is not directly counted, it is derived from MC by scaling with a luminosity factor.

$$N_{\text{total, Data}} = N_{\text{total, MC}} \times \frac{L_{\text{Data}}}{L_{\text{MC}}} \tag{4.7}$$

$$N_{\text{total, Data}} = N_{\text{total, MC}} \times \frac{52.11}{216.22} = 50702.6$$

One can also use the $e^+e^- \to \tau^+\tau^-$ cross section, 0.919nb and the data luminosity to predict the total number of Dalitz decays in data:

$$N_{\text{total, data}} = 0.919\text{nb} \times L_{data} \times \text{BF}(\tau \to h\pi^0) \times \text{BF}(\tau \to \mu) \times \text{BF}(\pi^0 \to e^+e^-\gamma) \times 2 \tag{4.8}$$

The efficiency and purity calculations confirms a well-controlled selection process. The purity before applying the final selection cuts was 43% with an ϵ of 8%. We take a hit on the ϵ at 1.22% while achieving high purity of 99.27% of Dalitz sample after final cuts, this is the *trade-off*. The Dalitz decay BF is measured to be 0.01076 ± 0.00045(stat.) compared to the PDG value of 0.01174 ± 0.00035. Measuring a BF consistent within stat errors of the PDG validates the detector MC's description of the data.

The final requirements, tightening the constraints on the transverse momentum of the electron and positron >0.3GeV helps ensure the tracks make it to the ECL so that the ECL is used in PID, the transverse displacement from conversions <0.5cm suppresses the conversion in material backgrounds and transverse displacement cut <1cm removes more conversion and mis-reconstructed Dalitz decays and background. The final discrepancy of 1.7σ suggests consistency between the data and the MC prediction, supporting the robustness of the selection criteria and analysis methodology.

Chapter 5

Systematics to be studied

This chapter provides guildlines for future work for building on the already existing analysis.

Firstly, to extract the BF of the Dalitz decay mode $\pi^0 \to e^+e^-\gamma$, one can normalize it using the well-measured two-photon decay mode $\pi^0 \to \gamma\gamma$ as a normalization mode. Using this approach, systematic and statistical uncertainties related to production and reconstruction largely cancel, improving the precision of the measurement.

Secondly, in principle, one can do a search for dark photon, with light quark (π^0) in initial state. But a crucial necessity is good resolution in the A' mass. This can be implemented by applying the `vertexTreefit` with an `ipConstraint` requirement on the selected Dalitz sample, this will ensure that the observed e^+e^- are reconstructed from the interaction point, this is significant as it is a prompt decay.

Lastly, one would have to finish the systematic studies to account for the full uncertainty on the measurement of the Dalitz decay BF. This is outlined in the next section.

5.1 Systematics

The results presented in the previous chapter are without including systematic uncertainties. So accounting for the systematic uncertainties is an important next step in determining the precise value of the Dalitz decay BF. A nonexhaustive list of studies as a starting point to probe these uncertainties is given below.

1. Particle identification (PID) performance
2. Momentum scale and resolution
3. Electromagnetic (EM) energy scale and resolution
4. Angular scale resolution

5. Conversion in material
    - Amount of material
6. Luminosity measurement uncertainty
7. Beam energy uncertainty
8. Theoretical uncertainties on
    - cross-sections
    - branching fractions
9. Background control improvements
    - various other probes for background studies
    - degree of control for the background

Items 6 and 8 can be computed readily by accounting for the following uncertainties:

- Total integrated luminosity measured at Belle II= (427.87 ± 2.01) fb^{-1} [58]
- $e^+e^- \to \tau^+\tau^-$ cross section=(0.919±0.003)nb
- $\tau \to \mu$ branching fraction=(17.39±0.04)%
- $\tau \to h\pi^0$, where h is a charged pion or kaon, branching fraction=(25.93±0.09)%.

Adding these in quadrature gives an additional relative uncertainty on the BF of 0.71%. The relative MC statistical error on the efficiency from these studies is 2.0% from Eq.4.6. Assuming a 100% uncertainty from background events corresponds to a relative uncertainty on the BF of 0.74%. Adding these in quadrature gives an estimated relative systematic uncertainty, excluding the systematic uncertainty on the efficiency, of 2.2%. Once systematic studies are completed the full dataset can be unblinded to perform final measurements.

Chapter 6

Conclusion

This study focused on measuring the Dalitz decay BF while validating MC simulations against real experimental data at Belle II. The Dalitz decay of the neutral pion, $\pi^0 \to \gamma e^+ e^-$, serves as a control process for dark photon searches. The Dalitz decay BF was measured to be:

$$BF(\pi^0 \to \gamma e^+ e^-) = 0.01076 \pm 0.00045(stat.)$$

This result is in good agreement with the PDG world average of

$$0.01174 \pm 0.00035$$

with a discrepancy of 1.7σ, validating the robustness of the selection and background suppression methods. The measured value of the BF takes into account only the statistical uncertainties, systematic studies must be taken into account before unblinding data to get a full BF measurement.

Moreover, the A' transverse vertex distribution showed misreconstruction of vertices of events with a bias towards the PXD when compared to generator level truth information. The A' transverse vertex distribution assuming its a converted photon proved to be significant in suppressing conversion backgrounds.

The efficiency in MC was found to be 0.0122±0.0002. The primary cause of efficiency loss stemmed from final selection cuts, which, while effectively suppressing background, also reduced the signal. In particular, cuts on transverse displacement and transverse displacement from conversions were crucial for rejecting misreconstructed Dalitz and non Dalitz decays at the PXD but also contributed to signal loss by eliminating events with displaced vertices due to imperfect vertex reconstruction. And we reject a lot of events with cuts on electron-positron tracks with transverse momentum > 0.3GeV.

These findings not only enhance confidence in Belle II's MC simulations but also highlight the need for improved vertex reconstruction algorithms to minimize systematic biases. Addressing these challenges will be essential for precision measurements of BF of decays and potential discoveries beyond the Standard Model.

Bibliography

[1] W. N. Cottingham and D. A. Greenwood, *An Introduction to the Standard Model of Particle Physics*. Cambridge University Press, 2007.

[2] D. H. Perkins, *Introduction to High Energy Physics*. Cambridge University Press, 2000.

[3] S. Navas *et al.*, "Review of particle physics," *Phys. Rev. D*, vol. 110, no. 3, p. 030001, 2024.

[4] D. Griffiths, *Introduction to Elementary Particles*. Wiley-VCH, 2008.

[5] CERN, "LHCb discovers three new exotic particles." https://home.cern/news/news/physics/lhcb-discovers-three-new-exotic-particles. Accessed: 2025-02-16.

[6] F. Halzen and A. Martin, *Quarks & Leptons: An introductory course in modern particle physics*. John Wiley & Sons, 1984.

[7] CERN, "The higgs boson: a landmark discovery." https://atlas.cern/Discover/Physics/Higgs. [Online; accessed: 16-Feb-2025].

[8] ATLAS Collaboration, "Observation of a new particle in the search for the Standard Model Higgs boson with the ATLAS detector at the LHC," *Phys. Lett. B*, vol. 716, no. 1, pp. 1–29, 2012.

[9] CMS Collaboration, "Observation of a new boson at a mass of 125 GeV with the CMS experiment at the LHC," *Phys. Lett. B*, vol. 716, no. 1, pp. 30–61, 2012.

[10] R. L. Workman *et al.* [Particle Data Group], "Review of Particle Physics," *Progress of Theoretical and Experimental Physics*, vol. 2022, p. 083C01, 2022.

[11] M. L. Perl *et al.*, "Evidence for Anomalous Lepton Production in e+ - e- Annihilation," *Phys. Rev. Lett.*, vol. 35, pp. 1489–1492, 1975.

[12] A. Pich, "Lessons learnt from the heavy tau lepton," *Cern Courier: Higgs and Electroweak*, 2000.

[13] D. Bodrov, "Tau physics at Belle and Belle II," *Int. J. Mod. Phys. A*, vol. 39, 2024.

[14] C. R. Nave, "Hyperphysics." http://hyperphysics.phy-astr.gsu.edu/hbase/Particles/meson2.html. [Online; accessed: 15-Feb-2025].

[15] H. Yukawa, "On the Interaction of Elementary Particles I," *Proceedings of the Physico-Mathematical Society of Japan*, vol. 17, pp. 48–57, 1935.

[16] H. Yukawa, S. Sakata, and M. Taketani, "On the Interaction of Elementary Particles III," *Proceedings of the Physico-Mathematical Society of Japan*, vol. 20, pp. 319–340, 1938.

[17] C. M. G. Lattes, G. P. S. Occhialini, and C. F. Powell, "Processes Involving Charged Mesons," *Nature*, vol. 160, pp. 453–456, 1947.

[18] C. Y. Chao, "Mixed Cosmic-Ray Showers at Sea Level," *Physical Review*, vol. 75, pp. 581–590, Feb 1949.

[19] J. Steinberger, W. K. H. Panofsky, and J. Steller, "Evidence for the Production of Neutral Mesons in Proton-Proton Collisions," *Physical Review*, vol. 78, pp. 802–806, Jun. 1950.

[20] R. Bjorklund, W. E. Crandall, B. J. Moyer, and H. K. Ticho, "Neutral Pion Lifetime and Decay Modes," *Physical Review*, vol. 77, no. 5, pp. 787–795, 1950.

[21] R. H. Dalitz, *Zero-zero transitions in nuclei*. PhD thesis, University of Cambridge, 1950.

[22] G. Bertone and D. Hooper, "A History of Dark Matter," *Reviews of Modern Physics*, vol. 90, no. 4, p. 045002, 2018.

[23] Epicurus, *Letter to Herodotus*, vol. 2. Harvard University Press, c. 305 BCE. Extracted from *Lives of Eminent Philosophers*, Translated by R. D. Hicks, 1925.

[24] I. Newton, *Philosophiæ Naturalis Principia Mathematica*. London, UK: Royal Society, 1687.

[25] H. Poincaré, "The Milky Way and Theory of Gases," *Revue Générale des Sciences Pures et Appliquées*, vol. 17, pp. 363–368, 1906. Originally published in French as "La Voie Lactée et la Théorie des Gaz".

[26] J. Kapteyn, "First Attempt at a Theory of the Arrangement and Motion of the Sidereal System," *Astrophysical Journal*, vol. 55, pp. 302–327, 1922.

[27] F. Zwicky, "Die Rotverschiebung von extragalaktischen Nebeln [The red shift of extragalactic nebulae]," *Helvetica Physica Acta*, vol. 6, pp. 110–127, 1933.

[28] V. C. Rubin and W. K. Ford Jr., "Rotation of the Andromeda Nebula from a Spectroscopic Survey of Emission Regions," *The Astrophysical Journal*, vol. 159, p. 379, 1970.

[29] E. Corbelli and P. Salucci, "The extended rotation curve and the dark matter halo of M33," *Monthly Notices of the Royal Astronomical Society*, vol. 311, pp. 441–447, Jan 2000.

[30] D. Clowe, M. Bradač, A. H. Gonzalez, M. Markevitch, S. W. Randall, C. Jones, and D. Zaritsky, "A Direct Empirical Proof of the Existence of Dark Matter," *The Astrophysical Journal*, vol. 648, p. L109, aug 2006.

[31] B. Koberlein, "Three Peaks at the Big Bang." https://briankoberlein.com/blog/three-peaks-big-bang/. Accessed: 2025-03-06.

[32] J. Willis, "ASTR405-The Cosmic Microwave Background." https://www.astro.uvic.ca/~jwillis/teaching/astr405/astr405_lecture3.pdf. Accessed: 2025-03-06.

[33] N. Aghanim *et al.* [Planck Collaboration], "Planck 2018 results. VI. Cosmological parameters," *Astronomy & Astrophysics*, vol. 641, p. A6, 2020.

[34] M. Graham, C. Hearty, and M. Williams, "Searches for Dark Photons at Accelerators," *Annual Review of Nuclear and Particle Science*, vol. 71, p. 37–58, Sept. 2021.

[35] B. Holdom, "Two U(1)'s and charge shifts," *Physics Letters B*, vol. 166, no. 2, pp. 196–198, 1986.

[36] A. J. Krasznahorkay, M. Csatlós, L. Csige, Z. Gácsi, J. Gulyás, M. Hunyadi, I. Kuti, B. M. Nyakó, L. Stuhl, J. Timár, T. G. Tornyi, and Z. Vajta, "Observation of Anomalous Internal Pair Creation in ^{8}Be: A Possible Indication of a Light, Neutral Boson," *Phys. Rev. Lett.*, vol. 116, no. 4, p. 042501, 2016.

[37] NA64 Collaboration, "Search for pseudoscalar bosons decaying into e^+e^- pairs in the NA64 experiment at the CERN SPS," *Physical Review D*, vol. 104, no. 11, p. L111102, 2021.

[38] NA62 Collaboration, "Search for K decays into the $\pi^+e^+e^-e^+e^-$ final state," *Physics Letters B*, vol. 846, p. 138193, 2023.

[39] K. Afanaciev *et al.* [MEG II collaboration], "Search for the X17 particle in $^7\mathrm{Li}(\mathrm{p}, \mathrm{e}^+\mathrm{e}^-)^8\mathrm{Be}$ processes with the MEG II detector," *arXiv preprint arXiv:2411.07994*, 2024.

[40] J. R. Batley *et al.*, "Search for the dark photon in π^0 decays," *Phys. Lett. B*, vol. 746, pp. 178–185, 2015.

[41] F. Forti *et al.* [Belle II Upgrades Working Group], "The Belle II Detector Upgrades Framework Conceptual Design Report," Jun 2024.

[42] "Superkekb project: Final design parameters." https://www-superkekb.kek.jp/. Accessed: 2024-06-26.

[43] E. Kou *et al.* [Belle II Collaboration], "The Belle II Physics Book." http://dx.doi.org/10.1093/ptep/ptz106, Dec. 2019.

[44] C. Praz, "Tracking performance and interaction point properties at the Belle II experiment." https://indico.cern.ch/event/895924/contributions/4018211/attachments/2104873/3561313/tracking_vertex2020_cyrille_praz_v5.pdf. Accessed: 2024-08-01.

[45] Belle II, "Inner and Tracking Detectors." https://belle2.jp/inner-and-tracking-detectors/. Accessed: 2024-06-26.

[46] W. Zihan, "The Silicon Vertex Detector of the Belle II Detector." https://docs.belle2.org/record/3802/files/BELLE2-TALK-CONF-2023-114.pdf. Accessed: 2024-08-01.

[47] W. Ahmed, "Material Budget Studies for the Belle II Detector," Master's thesis, McGill University, July 2017.

[48] T. Abe *et al.* [Belle II Collaboration], "Belle II Technical Design Report." https://arxiv.org/abs/1011.0352, 2010.

[49] R. Pestotnik, I. Adachi, R. Dolenec, K. Hataya, S. Iori, S. Iwata, H. Kakuno, R. Kataura, H. Kawai, H. Kindo, T. Kobayashi, S. Korpar, P. Križan, T. Kumita, M. Mrvar, S. Nishida, K. Ogawa, S. Ogawa, L. Šantelj, T. Sumiyoshi, M. Tabata, M. Yonenaga,

and Y. Yusa, "The aerogel Ring Imaging Cherenkov system at the Belle II spectrometer," *Nuclear Instruments and Methods in Physics Research Section A: Accelerators, Spectrometers, Detectors and Associated Equipment*, vol. 876, pp. 265–268, 2017. The 9th international workshop on Ring Imaging Cherenkov Detectors (RICH2016).

[50] P. Feichtinger, *Test of light-lepton universality in tau decays with data from the Belle II experiment*. PhD thesis, University of Vienna, 2024.

[51] T. Kuhr, C. Pulvermacher, M. Ritter, T. Hauth, and N. Braun, "The Belle II Core Software," *Computing and Software for Big Science*, vol. 1, no. 1, p. 1, 2018.

[52] Belle II Collaboration, "Data Main Page." https://xwiki.desy.de/xwiki/bin/view/BI/Belle%20II%20Internal/Data%20Production%20WebHome/Data%20main%20page/.

[53] S. Jadach, B. F. L. Ward, and Z. Wąs, "The Precision Monte Carlo Event Generator KK for Two-Fermion Final States in e+ e- Collisions," *Comput. Phys. Commun.*, vol. 130, no. 3, pp. 260–325, 2000.

[54] S. Agostinelli *et al.*, "GEANT4 – A Simulation Toolkit," *Nucl. Instrum. Methods Phys. Res. A*, vol. 506, no. 3, pp. 250–303, 2003.

[55] Belle II Software Group, "EventShape." https://software.belle2.org/development/sphinx/analysis/doc/EventShape.html#analysis-eventshape.

[56] Belle II Software Group, "Continuum suppression." https://software.belle2.org/development/sphinx/analysis/doc/ContinuumSuppression.html.

[57] J.-F. Krohn, F. Tenchini, P. Urquijo, F. Abudinén, S. Cunliffe, T. Ferber, M. Gelb, J. Gemmler, P. Goldenzweig, T. Keck, I. Komarov, T. Kuhr, L. Ligioi, M. Lubej, F. Meier, F. Metzner, C. Pulvermacher, M. Ritter, U. Tamponi, and A. Zupanc, "Global decay chain vertex fitting at Belle II," *Nuclear Instruments and Methods in Physics Research Section A: Accelerators, Spectrometers, Detectors and Associated Equipment*, vol. 976, p. 164269, 2020.

[58] Belle II Collaboration, "Measurement of the integrated luminosity of data samples collected during 2019–2022 by the Belle II experiment," *Chinese Physics C*, vol. 49, no. 1, p. 013001, 2025.

Appendix A

Additional Information

A.1 Steering script

The steering script used in this analysis is presented below.

```
import argparse
def argparser():

    parser = argparse.ArgumentParser(description=__doc__,
                                     formatter_class=argparse.
                                         RawTextHelpFormatter)

    parser.add_argument("--release",
                        type=int,
                        default=6,
                        help="The major release number associated to the
                            corrections that are being applied.\n"
                        "Default: %(default)s.")
    parser.add_argument("--global_tag_append",
                        type=str,
                        nargs="+",
                        default=['analysis_tools_light-2405-quaxo'],
                        help="List of names of conditions DB global tag(s) to
                            append on top of GT replay.\n"
                        "NB: these GTs will have lowest priority over GT
                            replay.\n"
                        "The order of the sequence passed determines the
                            priority of the GTs, w/ the highest coming first.\
                            n"
                        "Pass a space-separated list of names.\n"
                        "Default: %(default)s.")
```

```
21      parser.add_argument("--lid_weights_gt",
22                          type=str,
23                          default="leptonid_Moriond2023_Official_rel6_v0b",
24                          help="Name␣of␣conditions␣DB␣global␣tag␣with␣
                                recommended␣lepton␣ID␣correction␣factors.\n"
25                          "Default:␣%(default)s.")
26
27      return parser
28
29  args = argparser().parse_args()
30
31  import basf2 as b2
32  import modularAnalysis as ma
33  from variables import variables
34  import variables.collections as vc
35  import variables.utils as vu
36  import vertex
37  import pdg
38  from stdCharged import stdE, stdMu
39  # from variables.MCGenTopo import mc_gen_topo
40
41  pdg.add_particle("Ap", 53, 0., 0., 0, 0)
42
43  myPath = b2.create_path()
44  inputPath =[]
45  ma.inputMdstList(environmentType='default', filelist=inputPath, path=myPath)
46
47  trackCuts = 'dr␣<=␣1.0␣and␣-5.0␣<=␣dz␣<=␣5.0␣and␣nCDCHits␣>␣0'
48  gammaCuts = 'E␣>␣0.200␣and␣-0.8660␣<␣cosTheta␣<␣0.9563'
49
50  # for pion lets not apply any correction
51
52  ma.fillParticleList('e+:good', trackCuts, path=myPath)
53  ma.fillParticleList('mu+:good', trackCuts, path=myPath)
54  ma.fillParticleList('pi+:good', trackCuts, path=myPath)
55  ma.fillParticleList('gamma:good', gammaCuts, path=myPath)
56
57  my_particle_list=['e+:good','mu+:good','pi+:good']
58  b2.conditions.prepend_globaltag('tracking_data_Moriond23_v1')
59  ma.scaleTrackMomenta(inputListNames=my_particle_list,
60                           payloadName='tracking_momentumScaleFactor_global',
61                           scalingFactorName='sf_global_central', #sf_global_up,
```

```
                                sf_global_down
62                          path=myPath)
63
64  muons_wp = "FixedThresh095"
65  muon_id_var, muon_id_weights = stdMu(muons_wp, "likelihood", "global", args.
        lid_weights_gt,
66                                       release=args.release,
67                                       inputListName="mu+:good",
68                                       outputListLabel="lh_G_fixed095",
69                                       path=myPath)
70
71
72  Atomki_cut = f"[nCleanedTracks({trackCuts}) == 4] and [nParticlesInList(gamma:
        good) == 1]"
73  ma.applyEventCuts(Atomki_cut, path=myPath)
74
75  (pi0Min, pi0Max) = (0.08, 0.2)
76  ma.reconstructDecay('Ap:ee -> e+:good e-:good','',path=myPath)
77  ma.reconstructDecay('pi0:dalitz -> Ap:ee gamma:good', '%s < M < %s' % (pi0Min,
         pi0Max), path=myPath)
78
79  ma.reconstructDecay('tau+:signal -> pi0:dalitz pi+:good', 'M < 1.8', path=
        myPath)
80
81  ma.reconstructDecay('tau-:tag -> mu-:lh_G_fixed095', '', path=myPath)
82  ma.reconstructDecay('vpho:all -> tau+:signal tau-:tag', '', path=myPath)
83
84  #vertex fitting
85  vertex.treeFit('Ap:ee', ipConstraint=False, conf_level=0, updateAllDaughters=
        True, path=myPath)
86
87  ma.buildEventShape(['pi+:good', 'gamma:good','e+:good','mu+:lh_G_fixed095'],
88                     thrust=True,
89                     foxWolfram=False,
90                     cleoCones=False,
91                     jets=False,
92                     harmonicMoments=False,
93                     allMoments=False,
94                     collisionAxis=False,
95                     sphericity=False,
96                     path=myPath)
97
```

```
98
99  ma.buildEventKinematics(['pi+:good', 'gamma:good','e+:good','mu+:lh_G_fixed095
        '],
100                         path=myPath)
101
102 #IDENTIFIED THIS AS ERROR AND CORRECTED IT
103 variables.addAlias('cosTheta1',
104                    'formula(daughter(0,␣daughter(0,␣cosToThrustOfEvent))*
                           daughter(1,␣daughter(0,cosToThrustOfEvent)))')
105 variables.addAlias('cosTheta2',
106                    'formula(daughter(0,␣daughter(1,␣cosToThrustOfEvent))*
                           daughter(1,␣daughter(0,cosToThrustOfEvent)))')
107
108 variables.addAlias('EoverP', 'formula(␣ifNANgiveX(␣clusterE,␣-1␣)/p␣)')
109 #calculating total energy of event
110 # variables.addAlias('ecmstausig','formula(((daughter(0, useCMSFrame(p)))
        ^2+(1.77686^2))^0.5)')
111 # variables.addAlias('ecmstautag','formula(((daughter(1, useCMSFrame(p)))
        ^2+(1.77686^2))^0.5)')
112 # variables.addAlias('totalE','formula(ecmstausig+ecmstautag)')
113
114 ma.applyCuts('vpho:all', 'cosTheta1␣<␣0␣and␣cosTheta2␣<␣0', path=myPath)
115 ma.applyCuts('vpho:all', 'charge␣==␣0', path=myPath)
116 ma.applyEventCuts("[L1Trigger==1]␣and␣[HighLevelTrigger==1]", path=myPath)
117
118 ma.matchMCTruth('tau+:signal', path=myPath)
119 ma.matchMCTruth('tau-:tag', path=myPath)
120
121 # Get information of the generated decay mode calling labelTauPairMC from
        modular analysis
122 ma.labelTauPairMC(TauolaBelle=True, path=myPath)
123 # Store some useful event variables, as the thrust, the event kinematics
        variables.
124 eventVariables = ['EoverP','clusterE','thrust',
125                   'visibleEnergyOfEventCMS',
126                   'missingMomentumOfEvent',
127                   'missingMomentumOfEvent_theta',
128                   'missingMomentumOfEventCMS',
129                   'missingMomentumOfEventCMS_theta',
130                   'totalPhotonsEnergyOfEvent',
131                   'missingMass2OfEvent',
132                   'tauPlusMCMode',
```

```
133                     'tauMinusMCMode',
134                     'charge','E','pt','useCMSFrame(E)','useCMSFrame(pt)']
135
136 # Store also some useful MC match information.
137 mcVariables = vc.mc_variables
138
139 # You can use collections of variables, as vc.kinematics or vc.inv_mass.
140 kVariables = vc.inv_mass + vc.kinematics
141
142 convertedPhotonvars = ["convertedPhotonDelR(0,1)", "
        convertedPhotonDelTanLambda(0,1)",
143                        "convertedPhotonDelZ(0,1)",
144                        "convertedPhotonInvariantMass(0,1)",
145                        "convertedPhotonPx(0,1)",
146                        "convertedPhotonPy(0,1)",
147                        "convertedPhotonPz(0,1)",
148                        "convertedPhotonRho(0,1)",
149                        "convertedPhotonX(0,1)",
150                        "convertedPhotonY(0,1)",
151                        "convertedPhotonZ(0,1)"]
152
153 tauVariables = ['tauMinusMCMode', 'tauPlusMCMode', 'tauMinusMCProng', '
        tauPlusMCProng']
154 lid_mu = [muon_id_var] + muon_id_weights
155 ID_variables=['pionID','pionID_noSVD', 'muonID' ,'muonID_noSVD','
        electronID_noSVD','electronID_noTOP','phi','dphi','firstPXDLayer']
156
157 # Here we will create the variable list
158 variableList = vu.create_aliases_for_selected(list_of_variables=eventVariables
        ,decay_string='^vpho') + \
159                vu.create_aliases_for_selected(list_of_variables=
                       convertedPhotonvars+["flightTime",'flightDistance','dr','
                       x_uncertainty','y_uncertainty'],
160                decay_string='vpho␣->␣[tau+␣->␣[pi0␣->␣[^Ap␣->␣e+␣e-]␣gamma]␣pi
                       +]␣[tau-␣->␣mu-]',prefix=['Ap']) + \
161                 vu.create_aliases_for_selected(list_of_variables=kVariables +
                        tauVariables + ['chiProb','mcDecayVertexRho','clusterEoP','
                        EoverP','clusterE','isSignalAcceptMissingNeutrino','
                        isSignal','isSignalAcceptMissingNeutrino','charge','
                        useCMSFrame(cosTheta)','useCMSFrame(E)','useCMSFrame(pt)','
                        useCMSFrame(px)','useCMSFrame(py)','useCMSFrame(pz)','
                        cosTheta','distance','x','y','nPXDHits','electronID']+
```

```
                    mcVariables,
162                 decay_string='vpho␣->␣[^tau+␣->␣[^pi0␣->␣[^Ap␣->␣^e+␣^e-]␣^
                    gamma]␣^pi+]␣[^tau-␣->␣^mu-]',prefix=['tau_sig','pi0','Ap',
                    'ep','em','gamma','pip','tau_tag','mu_tag'])+\
163             vu.create_aliases_for_selected(list_of_variables=ID_variables,
                    decay_string='vpho␣->␣[tau+␣->␣[^pi0␣->␣[Ap␣->␣^e+␣^e-]␣gamma]
                    ␣^pi+]␣[tau-␣->␣^mu-]',prefix=['pi0','ep','em','pip','mu_tag']
                    )+\
164             vu.create_aliases_for_selected(list_of_variables=lid_mu,
                    decay_string='vpho␣->␣[tau+␣->␣[pi0␣->␣[Ap␣->␣e+␣e-]␣gamma]␣pi
                    +]␣[tau-␣->␣^mu-]',prefix=['mu_tag']  )
165             # vu.create_aliases_for_selected(list_of_variables=lid_e,
                    decay_string='vpho -> [tau+ -> [pi0 -> [Ap -> ^e+ ^e-] gamma]
                    pi+] [tau- -> mu-]',prefix=['ep','em']  )
166
167
168 outputFile = 'after.root'
169
170 ma.variablesToNtuple(decayString='vpho:all',
171                      variables=variableList,
172                      filename=outputFile,
173                      treename='tau',
174                      path=myPath)
175
176 ma.variablesToNtuple(decayString='',
177                      variables=['nTracks'],
178                      filename=outputFile,
179                      treename='event',
180                      path=myPath)
181
182 b2.process(path=myPath)
183 print(b2.statistics)
```